Surface Study of Nickel Phosphide and Cobalt Sulfide Nanoparticles for Heterogeneous Catalysis

By

Stephanie Castillo

Thesis

Submitted to the Faculty of the

Graduate School of Vanderbilt University

in partial fulfillment of the requirements

for the degree of

MASTER OF SCIENCE

in

Chemistry

August 31, 2017

Nashville, Tennessee

Approved:

Janet E. Macdonald, Ph.D.

Timothy P. Hanusa, Ph.D.

ACKNOWLEDGMENTS

This work was supported financially by the Department of Chemistry at Vanderbilt University and the Graduate Assistance in Areas of National Need (grant number 9200A140248). Portions of this work were performed at the Vanderbilt Institute of Nanoscale Science and Engineering, using facilities under NSF EPS-1004083.

TABLE OF CONTENTS

LIST OF TABLES

Table Page

LIST OF FIGURES

Figure Page

CHAPTER 1

INTRODUCTION

1.1 Chemical Synthesis in Need of Novel Heterogeneous Catalysts

Chemicals are the building blocks for products that meet our most fundamental needs; food, shelter, health, and energy. The U.S. chemical industry alone manufactures and markets more than 70,000 distinct products and is the world's largest producer of chemicals.[1] The outstanding success of the chemical industry is largely due to scientific and technological advances, making new products and processes possible. Further research and development is needed in order for the U.S. chemical industry to continue leading the advancement of technology and meeting the needs of consumers. Three areas of interest that fall under "New Chemical Science and Engineering Technology" according to the American Chemical Society's *Technology Vision 2020* are (i) chemical synthesis, (ii) bioprocesses and biotechnology, and (iii) materials technology.[2]

This work will focus on chemical synthesis and materials technology. The current processes used in chemical synthesis depend heavily on catalysts to increase the fraction of molecules that are able to react, thus increasing the rate of the reaction. In terms of material technology, understanding the structure of materials at the nano to micro scale would help researchers develop techniques to increase catalytic performance. Therefore, by integrating material technology into chemical syntheses, catalytic nanomaterials could replace traditional catalysts, which are highly desirable in large-scale chemical processes.

A catalyst is a substance that can expedite the rate of a chemical reaction and is capable of maintaining activity via regeneration. Catalysts lower the energy of activation (E_a) in chemical reactions by providing an alternate chemical transition state to the reaction mechanism, illustrated in Figure 1.1. The rate constant, k, is defined by the Arrhenius equation 1.1, where A is a constant related to collision rates and RT is the average kinetic energy. There are two types of catalytic processes used in chemical synthesis: homogeneous and heterogeneous catalysis. Both types of

processes require catalysts that are typically composed of metals, as these catalysts must be able to withstand the extreme conditions (e.g., high temperature and pressure) of industrial processes.

$$k = Ae^{-E_a/RT} \tag{1.1}$$

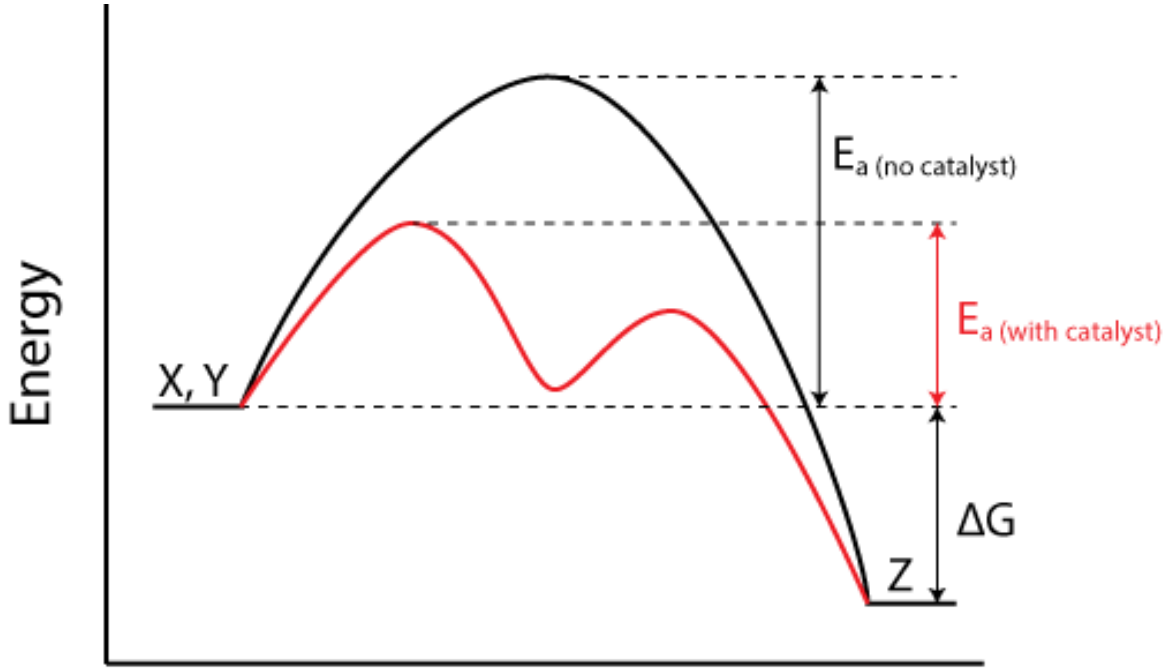

Figure 1.1. Energy diagram and the effect of a catalyst.

For homogenous catalysis, catalysts are in the same phase as the reactants and products, and are often organometallic complexes. In order to isolate the product at the end of a reaction, post-production processes are required for the separation of the catalysts from the products. This results in generation of excessive waste, making the overall system less environmentally friendly and economical. In heterogeneous catalysis, catalysts exist in a different phase and are generally bulk solids such as metals, metal oxides, or zeolites.[3] Heterogeneous catalysis has proven to be advantageous over homogeneous catalysis for chemical synthesis at the industrial scale, as it provides a relative ease of separation needed for catalytic regeneration.[4] Ideally, heterogeneous catalysts should be environmentally safe, affordable, and lead to a high product yield with minimal harmful by-products, but the current metal materials used are toxic and expensive with relatively high

life-cycle costs.

In heterogeneous catalytic reactions, the catalyst surface plays a critical role.[5] As shown in Figure 1.2, the first step of a heterogeneous catalytic reaction is the adsorption of reactants from the liquid/gas phase onto the solid catalyst surface. The absorbed species react with the atoms on the solid surface followed by desorption, releasing the products back into the liquid or gas phase. The surface sites where the reaction takes place are known as active sites. The greater the surface area, the more sites are available for catalytic reactions to take place. As a result, the catalytic activity is dependent on the surface area per unit mass.

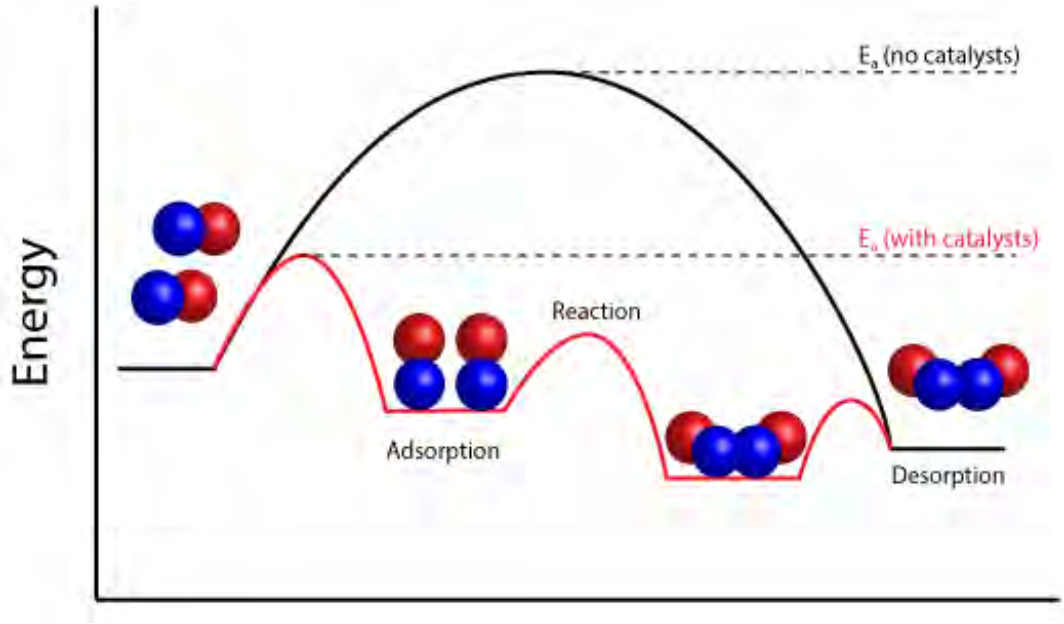

Figure 1.2. General heterogeneous catalytic reaction scheme.

Traditionally, heterogeneous catalysts have been made using simple synthetic routes with limited control over the size, shape, and composition of metal materials.[6] Bulk metals contain only a small concentration of surface atoms; as a result, broken chemical bonds on the exterior suppress the material's catalytic properties.[7] In order to increase the number of surface atoms, one can manipulate the surface-to-volume ratio, as it is inversely proportional to linear dimensions for any substance. As the size of the material decreases, the role of the surface becomes dominant because a larger percentage of the atoms are surface atoms. In the nanoscale regime (1-100 nm), surfaces

can significantly alter electrical, optical, magnetic, and chemical properties, and yield differences from their bulk counterparts.[8] Utilizing nanomaterials as catalysts for chemical synthesis could ultimately increase reaction rates, increasing production and product yield.

1.2 Integration of Nanomaterial Technology into Chemical Synthesis

Catalytic nanomaterials are gaining increasing attention, particularly compound metal nanoparticles (CMNPs), as they are thought to bridge the gap between metal complexes and heterogeneous bulk catalysts.[9] The preparation of NPs often rely on a "top-down" approach, where some bulk (precursor) material are subdivided into smaller units by numerous chemical and physical methods. In contrast, chemical procedures take a "bottom-up" approach in which controlled aggregation of atoms into particles is achieved by molecular precursors, a molecular stabilizer, and a reducing agent. The bottom-up approach allows for the ability to directly control size, shape, composition, and structure of catalysts and can potentially provide an efficient approach to the production of chemicals.[10] CMNPs have a large surface area-to-volume ratio, high concentration of low coordination sites, and surface vacancies that give rise to effective catalysts, which display efficiencies greater than or equal to bulk metal catalysts. Current CMNP catalysts are composed of late transition and noble metals, (e.g., Pt, Pd, Au, Rh, Ru) which are commonly stable in air, are durable at extreme temperatures, exhibit variable oxidation states, and can easily form or adsorb complexes due to partially-filled *d* orbitals. The late transition and noble metals low availability and high cost restricts their application in large-scale production. This has led to more efforts in the development of early transition metals for industrial heterogeneous catalysis.[11,12]

First-row transition metals are environmentally friendly and earth abundant, making them desirable as potential catalytic materials. These metals have unfilled *d* orbitals that allow them to exist in various oxidation states, which can initiate chemical changes in molecules that bind to their surface. Catalytic chemical reactions of CMNPs mainly include oxidation/reduction, coupling, and electrochemical reactions.[13] Metals and metal oxide NPs have dominated the catalytic field, but there has been a shift in interest to generate new catalytic materials as new processes

arise and the demand to improve existing processes grows. For example, metal carbides, nitrides, sulfides, and phosphides are becoming prominent in heterogeneous catalytic systems, but are still underdeveloped materials.[14,15] Carbides and nitrides have been made with 4*d*/5*d* metals like Mo, W, and Nb, whereas sulfides and phosphides have successfully been made with 3*d* metals such as Co, Fe, and Ni. These catalysts are usually used for oxidation, hydrogenation, coupling, and desulfurization reactions. In this work, we will be focused solely on nickel phosphide and cobalt sulfide NPs for their use as potential alternatives to current heterogeneous catalysts.

1.3 Research Motivation

The efficiency of a catalyst is estimated by turnover frequency per site per unit time (TOF). Homogeneous catalysts usually have a TOF greater than 1000 at temperatures around 100°C, whereas traditional heterogeneous catalysts have low TOF of less than 100.[16] Achieving a TOF closer to those of homogenous catalysts while still retaining easy separation similar to that of heterogeneous catalysts is the standard in making an efficient CMNP catalysts. The catalytic properties of CMNPs, which change with variations of size and shape, may change the TOF due to a combination of localized coordination effects, surface site distribution, surface relaxation, and quantum size effects.[17] CMNPs have been synthesized through the separation of nucleation and growth processes, producing CMNPs of various size and shapes.[8,18,19] Controlling the morphology of CMNPs translates into the ability to control the exposure of crystal facets and the number of atoms on corners and edges, and thus the ability to tune the activity and selectivity of a catalytic system.[20] The facets provide various metal coordination sites on the CMNPs that can exhibit different coordination chemistry towards reactants, intermediates, and products.[21] High-index facets exhibit superior reactivities in heterogeneous catalysis due to their high-surface energy active sites, which facilitate rapid bond cleavage and bond generation.[22]

The CMNPs shape and facet exposure can be controlled during growth by ligands, surfactants, or polymers coordinating to specific facets, minimizing the surface energy, and ultimately changing the surface environment of the CMNPs.[23] These capping agents can either bond datively,

covalently, or ionically, providing electrostatic or static stability and solubility in polar or nonpolar media; stability is needed for further processing and application.[24] Traditionally, CMNPs are immobilized onto inorganic or organic polymer supports as they are usually lower in stability in comparison with bulk catalysts.[25] This is a problem, as it decreases surface area and hampers the catalytic activity of the CMNPs. When used without a support, capping agents can act as a physical barrier to the reactants by restricting accessibility to the catalytically active metal sites on the CMNPs surface.[26] The proposed solution to these problems is to access another ligand binding mode where the ligand is in a higher coordination site within the crystal lattice of the CMNPs, subsequently increasing stability and diminishing the need for an exterior support; this binding mode is called "crystal-bound."[27]

Typically, ligands for NPs have long alkyl chains that are attached to a polar head group of either phosphines, oxides, carboxylic acids, amines, or thiols. In the synthesis of NPs with crystal-bound ligands, the ligand plays the role of the NP stabilizer and anion source. This crystal-bound ligands allows the metal sites to be available, as the alkyl chains are directly attached to the anion and form a terminal layer that provides stability and solubility of CMNPs in organic media (Figure 1.3).[28] When using surfactants or ligands that are datively bound, the ligands are susceptible to removal during purification of the CMNPs; this type of binding mode is referred as "surface-bound."[29] Surface-bound ligands are also likely to detach during a reaction, causing agglomeration to occur making the MNPs ineffective. For industrial usage, the stability, sustainability, and recyclability are evaluated in order to determine the efficiency of CMNPs as catalysts for chemical synthesis. With crystal-bound ligands, all three criteria can be met, increasing the efficiency of CMNPs as catalysts for heterogeneous chemical synthesis.

Although well-defined CMNPs with high-index facets, and uniform size and shape have already been established and well-studied, there is still a lack of control on the binding mode of the ligands, characterization of the ligands present on the surface of NPs, and experimental studies on the effect of ligands on the catalytic activity at the atomic scale. Before CMNPs can be applied as catalysts, their surfaces must be well-characterized and well-defined, as heterogeneous catalysis is

a surface-dependent reaction.

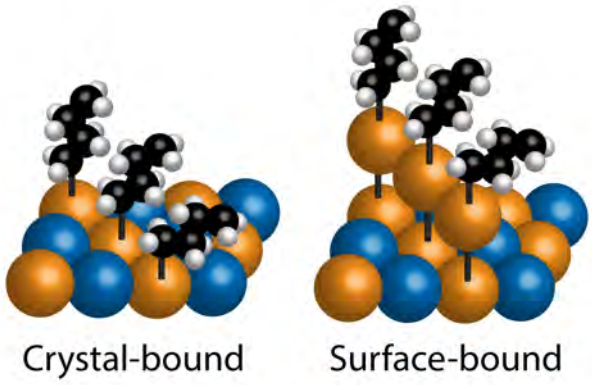

Figure 1.3. General illustration of the two binding modes of ligands on metal anion nanoparticle surface.

To the best of our knowledge, a detailed study on the surface characterization of nickel phosphide and cobalt sulfide NPs has yet to be reported. Previous studies have implemented these materials into heterogeneous catalytic reactions, without considering how the ligands on the surface affect the catalytic activity. In this work, the synthesis of nickel phosphide and cobalt sulfide NPs in solvothermal reactions are described, where tertiary phosphine and primary thiol ligands are used to target crystal-bound Ni_2P and Co_2S NPs. In Chapter 2, a detailed account of the characterization of Ni_xP_y NPs is presented, and whether the type of phosphine ligand affects their morphology, composition, shape, and structure is discussed. To determine if the phosphine ligands were crystal-bound, proton nuclear magnetic resonance (^{1}H NMR) spectroscopy was used, followed by ligand exchange. A temperature-dependent study was also carried out in an attempt to induce incorporation of the phosphine ligands into the crystal lattice at lower temperatures. In Chapter 3, a preliminary study of the catalytic activity of cobalt sulfide is explored via linear sweep voltammetry. The surface of cobalt sulfide particles is characterized by ^{1}H NMR and Fourier Transform Infrared Spectroscopy (FTIR).

CHAPTER 2

UNDERSTANDING THE SURFACE CHEMISTRY OF NICKEL PHOSPHIDE NANOPARTICLES FOR HETEROGENEOUS CATALYSIS

2.1 Introduction

The development of an affordable, sustainable, and environmentally clean heterogeneous catalysts is a persistent challenge in the production of chemicals. Interest in nickel phosphide NPs has continued to grow as it exhibits high catalytic activity and resistance to poisoning.[30] The relatively strong Ni–P bonds increases the thermal stability and hardness of the material comparable with that of hardened high carbon steels, as well as resistance to oxidation and chemical attack over the metal.[31] The catalytic activity of Ni_xP_y NPs has been tested for water splitting,[32,33] water oxidation,[34,35] hydrogen evolution,[36–40] hydrodeoxygenation,[41,42] and hydrodesulfurization processes.[12,43,44] Ni_xP_y NPs that are metal rich are better candidates for heterogeneous catalysis, displaying a metallic behavior, whereas phosphorous rich Ni_xP_y NPs behave as semiconductors.[45,46]

The most predominant Ni_xP_y NPs used for heterogeneous catalysis are Ni_2P NPs whose crystal structure has been thoroughly characterized through several studies. Ni_2P adopts a hexagonal structure[47] where Ni–Ni bonds are only slightly elongated compared to the Ni–Ni bonds of face-centered cubic Ni, with short Ni–P bonds (Figure 2.1).[15] The structure of bulk Ni_2P is composed of two alternating atomic layers, Ni_3P and Ni_3P_2, along the *c* direction, where the sum of the two layers gives the Ni_2P stoichiometry of the crystal (Figure 2.1b).[48] The Ni atoms hold two different coordination states: Ni(1) is tetrahedral and reported as the active center, and Ni(2) in the Ni_3P plane is square-pyramidal (Figure 2.1a).[48,49] The Ni_2P catalytic activity has been computationally studied and suggests that the Ni atoms become catalytically active by a small Ni $\rightarrow$ P charge transfer that occurs when the P atoms insert into the Ni structure, creating a weak ligand effect that allows for the dissociation of molecular hydrogen in hydrodesulfurization reactions.[50] Ni_2P NPs can bind strongly with reactants and moderately with products, where Ni atoms in hydrodesulfur-

ization reactions adsorb significant amounts of hydrogen, thus a good heterogeneous catalyst that can take the place of noble metal heterogeneous catalysts.[48,51]

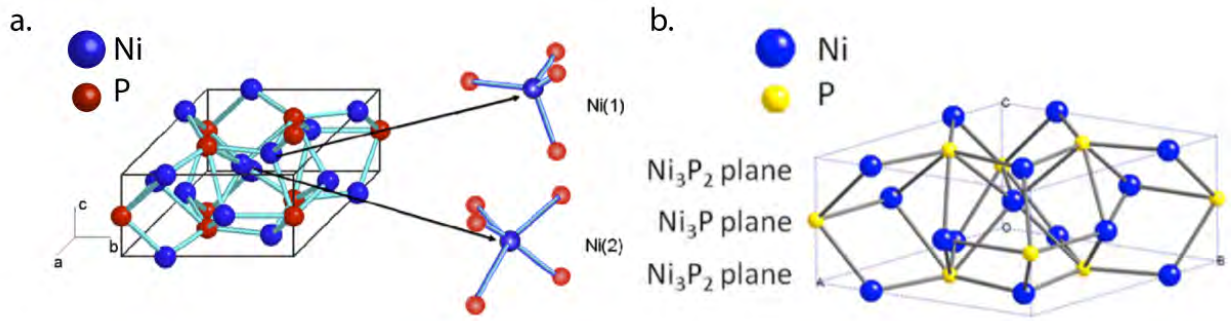

Figure 2.1. Hexagonal structure of Ni_2P; a.) different coordination states of Ni and b.) the Ni_3P and Ni_3P_2 planes that make up Ni_2P. Copyright Elsevier 2017. Copyright American Chemical Society 2017.

The Ni_2P NPs implemented into heterogeneous catalytic processes are pseudo-spherical and have been synthesized by hydrothermal,[11,12] solvothermal,[52–54] and organometallic decomposition[42,55–59] routes. Hydrothermal and solvothermal routes require extremely high temperatures along with the use of autoclaves, making it difficult to control the size and shape of the NPs. The organometallic decomposition route has proven to be more successful as it allows for the control of size, shape, and composition of Ni_2P NPs. A typical organometallic decomposition reaction includes a metal precursor, an anion source, and either a ligand or surfactant in the presence of a non-coordinating solvent. The metal precursors are mainly organometallic compounds or metal salts. The modification of the type of metal precursor, Ni/P ratio, phosphorus ligand and surfactant concentration, and temperature has produced pure phase Ni_2P NPs of various shapes and sizes with different catalytic activity.[42,55–57]

The thermal decomposition mechanism of Ni_2P NPs, Figure 2.2, begins with the decomposition of an organometallic Ni complex (or dissolution of metal salts) in the presence of excess phosphine ligands, which transitions into the nucleation of Ni–P seeds. At high enough temperatures (e.g., 300°C), phosphidation begins where P atoms diffuse into the Ni seeds causing the formation of Ni_xP_y phases. After an aging process of at least 2 h, pure phase Ni_2P NPs are formed. The formation of Ni_2P NPs is proposed to be dependent on the diffusion rates of Ni and P, but what is

interesting is the use of excess phosphine ligands.

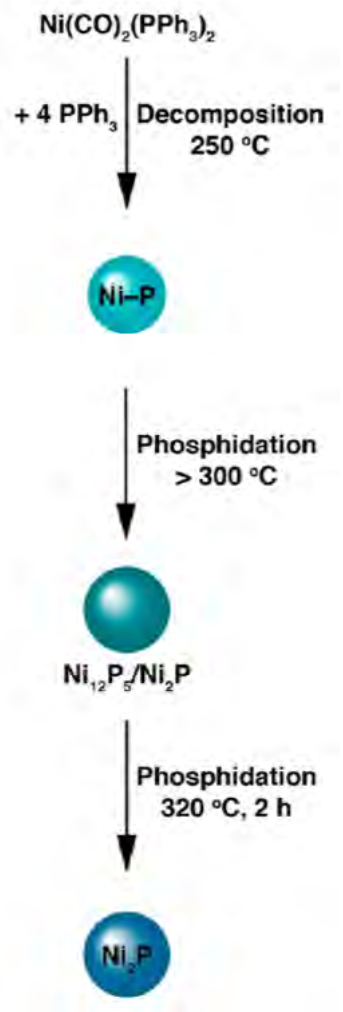

Figure 2.2. A general illustration of the mechanism of formation for Ni_2P NPs reported by Habas *et. al.*.Copyright Chemistry of Materials 2015.

It has been reported that when ligands are also the anion source, it results in crystal-bound ligands.[27,60] For instance, copper salt in the presence of alkane thiol ligands forms Cu_2S with crystal-bound ligands directly, without the formation of metallic copper NP intermediates. The major difference between Ni_2P and Cu_2S is Ni_2P forms through intermediate phases rather than directly, but since the phosphine ligands are also the anion source, will the mechanism of formation of Ni_2P result in crystal-bound ligands? The bonding of the ligand can potentially be of importance in the catalytic activity of Ni_2P NPs in heterogeneous processes. With crystal-bound ligands, the

anion atoms sit in high-coordination-number sites with the ligands still intact providing: (i) NP stability and robustness eliminating the need for a support; and (ii) the potential to increase catalytic activity, as there is an increased number of exposed metal atoms on the surface readily available in heterogeneous processes. If heterogeneous catalysis is a surface-dependent reaction, then a deep understanding of the chemistry occurring at the surface is required in order to better functionalize Ni_2P NP catalysts for specific roles. To the best of our knowledge, the surface characterization of Ni_2P NPs has yet to be reported.

In this chapter, the surface of Ni_2P NPs synthesized through a modified thermal decomposition route of the Ni carbonyl compound depicted in Figure 2.3 was explored.[42] ^{1}H nuclear magnetic resonance (NMR) spectroscopy was primarily utilized for the surface characterization of Ni_2P NPs in the presence of three different phosphine ligands: tributylphosphine (TBP), trioctylphosphine (TOP), and triphenylphosphine (TPP). The use of three distinct phosphine ligands were used in an effort to achieve NPs with crystal-bound ligands, and to determine if varying the alkyl chain length and functional group will affect the formation of crystal-bound ligands. Transmission electron microscopy (TEM), energy-dispersive X-ray spectroscopy (EDS), selected area electron diffraction (SAED), and X-ray diffraction (XRD) techniques were used to characterize the morphology, size, composition, and structure of the Ni_2P NPs.

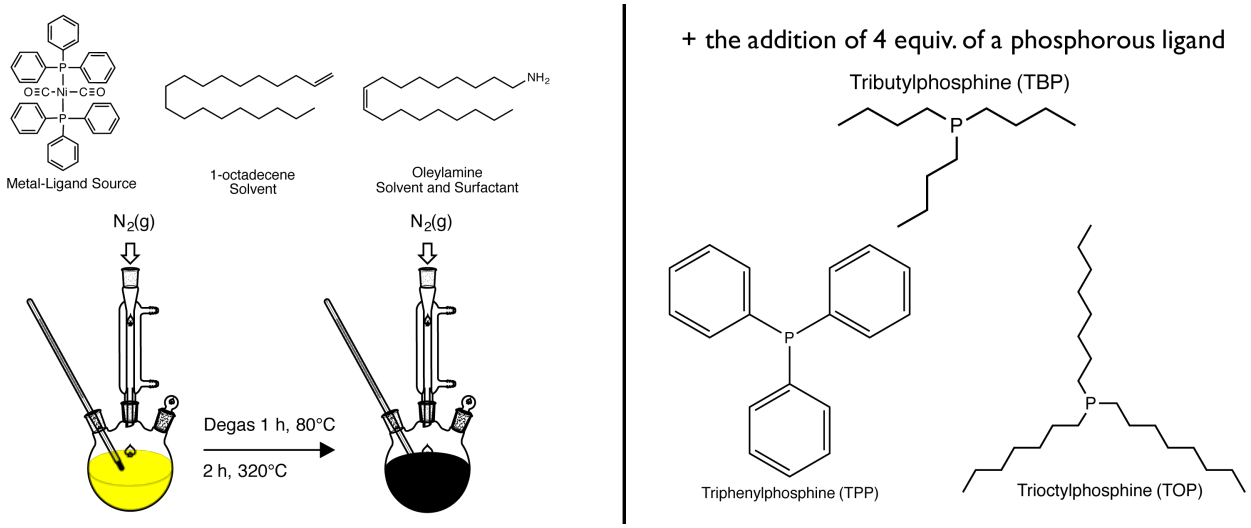

Figure 2.3. Schematic illustration of the synthesis of Ni_2P NPs

The effect of temperature was also evaluated in the interest of obtaining crystal-bound ligands at a lower temperature of reaction. The reaction temperature for thermal decomposition is at 320°C, well above the boiling point of the ligands, which may result to degradation and may be the primary factor for the phosphidation of P atoms into Ni_xP_y seeds. The reaction temperatures for this study ranged from 265–300°C; TEM, EDS, SAED, and XRD were used to track the morphology, composition, and phase of the Ni_2P NPs at each temperature; ^1H NMR was used to examine the surface of the Ni_xP_y NPs at each temperature.

2.2 Experimental Techniques

2.2.1 Materials

Oleylamine (OAm, 70%), 1-octadecene (ODE, 90%), trioctylphosphine (TOP, 90%), and bis-(triphenylphosphine)dicarbonylnickel(0) ($[Ni(CO)_2(PPh_3)_2]$, 99%) were purchased from Sigma-Aldrich. Triphenylphosphine (TPP, 99%) was purchased from Strem Chemicals. All chemicals were used as received without additional purification unless noted. Standard air-free Schlenk techniques was used throughout with N_2 as the inert gas.

2.2.2 General Synthesis of Ni_2P NPs

A Ni_2P synthesis was developed based on the work of Habas *et al.*[42] Ni_2P NPs were prepared via the reaction scheme shown in Figure 2.3. OAm (3.00 mL, 9.12 mmol), $[Ni(CO)_2(PPh_3)_2]$ (0.500 mmol), and a phosphorus ligand (2.00 mmol of TBP, TOP, or TPP) were added to ODE (3.00 mL) in a three-neck round-bottom flask. The reaction mixture was degased for 1 h at 80°C, and then increased to the desired temperature (265–320°C) under N_2 atmosphere. The temperature was maintained for 2 h and then cooled to ambient temperature by removal of the heat source. A 3.0 mL portion of chloroform was added to the reaction mixture in air followed by 15 min of sonication at 40°C. The NPs were precipitated by the addition of 20.0 mL of 2-proponal and 10.0 mL of ethanol, and separated via centrifugation at 8700 rpm for 10 min. The NPs were further

purified by repeated centrifugation and decantation three more times, with additions of methanol and minimal chloroform. NPs were stored in chloroform until further use.

2.2.3 Ligand Exchange

In a large 6 dram vial, a 50 μL portion of Ni_2P NPs was added drop-wise to a mixture of TPP (0.400 mmol) and chloroform (4.00 mL). The mixture was stirred for 1 h in air. A 10.0 mL portion of acetone was added, and then centrifuged at 4400 rpm for 10 min to separate NPs from solution. Supernatant was discarded and the NPs were dried under vacuum for 30 min in preparation for ^{1}H NMR.

2.2.4 Characterization & Instrumentation

Transmission electron microscopy (TEM) images were collected and energy dispersive X-ray spectroscopy (EDS) was carried out using a FEI Tecnai Osiris™ digital 200 kV S/TEM system. TEM samples were prepared by drop-casting a dilute NP solution in chloroform onto a copper grid with a carbon support and dried in air at room temperature. NPs sizes were determined manually using ImageJ with number of particles measured, n = 100. EDS spectra were collected for 2 min and quantified using the Espirit software. P content was quantified using the K series of peaks, while Ni content was quantified using the L series. All spectra were background subtracted and overlapping Ni sample and Cu grid peaks were deconvoluted before quantification. Drift-corrected EDS maps were collected for 90 s with beam current 1.5 nA. X-ray diffraction (XRD) measurements were performed using a Scintag XGEN-4000 X-ray diffractometer with a CuK_α (λ = 0.154 nm) radiation source. The resulting diffraction patterns were then visually compared to ICDD database and literature data to determine the structure.[42] The absorption spectra of NP samples were collected from 300–1000 nm on an ultraviolet-visible spectrophotometer (Jasco V-670) with an excitation wavelength of 348 nm. Samples were measured in solution with chloroform as the solvent. ^{1}H NMR spectra were recorded on Bruker DRX-400 (400 MHz) spectrometers. Spectra were calibrated to residual solvent signals of 7.26 ppm for ^{1}H NMR spectra in $CDCl_3$.

2.3 Results & Discussion

2.3.1 The Effect of Phosphine Ligands on the Size and Phase of Ni_2P NPs

The decomposition reaction of $[Ni(CO)_2(PPh_3)_2]$ in the presence of three different phosphine ligands at 320°C resulted in single phase Ni_2P NPs with of different NP size distributions. The functional group of the ligand does not affect the phase, as the SAED patterns of each reaction (Figure 2.5b,e,h) show single phase Ni_2P NPs and are in agreement with the 2θ reported in JCPDS 03-0953. This single phase is further supported by EDS, as the atomic ratio of Ni and P is roughly 2:1, respectively (Figure 2.4). The use of the shorter alkyl chained TBP led to monodispersed NPs (5.32 $\pm$ 0.69 nm), while the longer chained TOP led to polydispersed NPs(8.50 $\pm$ 2.00 nm) (Figure 2.5) in diameter. The aryl functional group on TPP resulted in larger monodispersed NPs than both TBP and TOP (25.90 $\pm$ 3.73 nm).

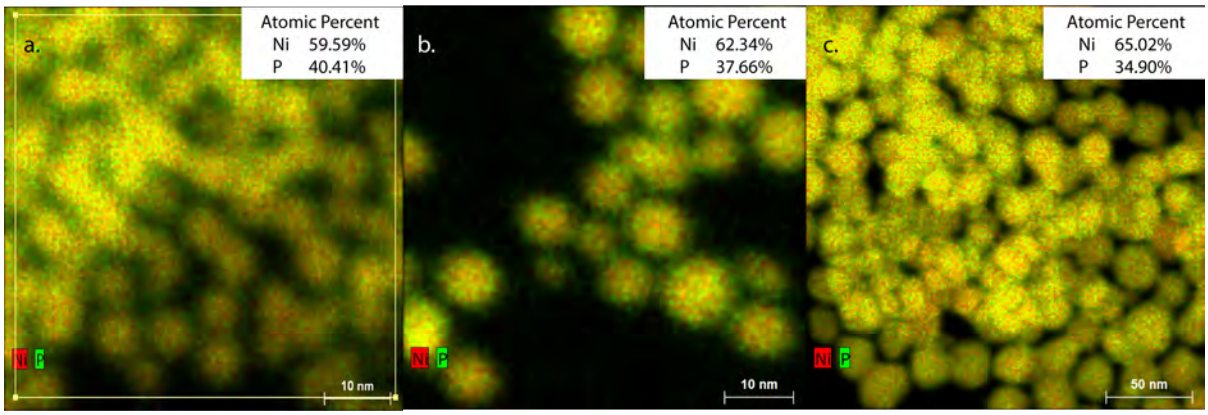

Figure 2.4. EDS map of Ni_2P when using a.) tributylphospine, b.) trioctylphosine, and c.) triphenylphosphine as phosphine ligands.

One possibility for the difference in sizes of the resultant NP product between the phosphine ligands could either pertain to P–C bond strength or steric bulk of the functional group. Generally, the longer the P–C bond length, the weaker the P–C bond, the greater the chance for P–C bond cleavage to occur resulting in an increase in size. This may be true for the drastic size difference between TOP and TPP, but would not explain the size difference between TOP and TBP as their bond strengths are relatively the same. To determine if cleavage is occurring, gas chromatography

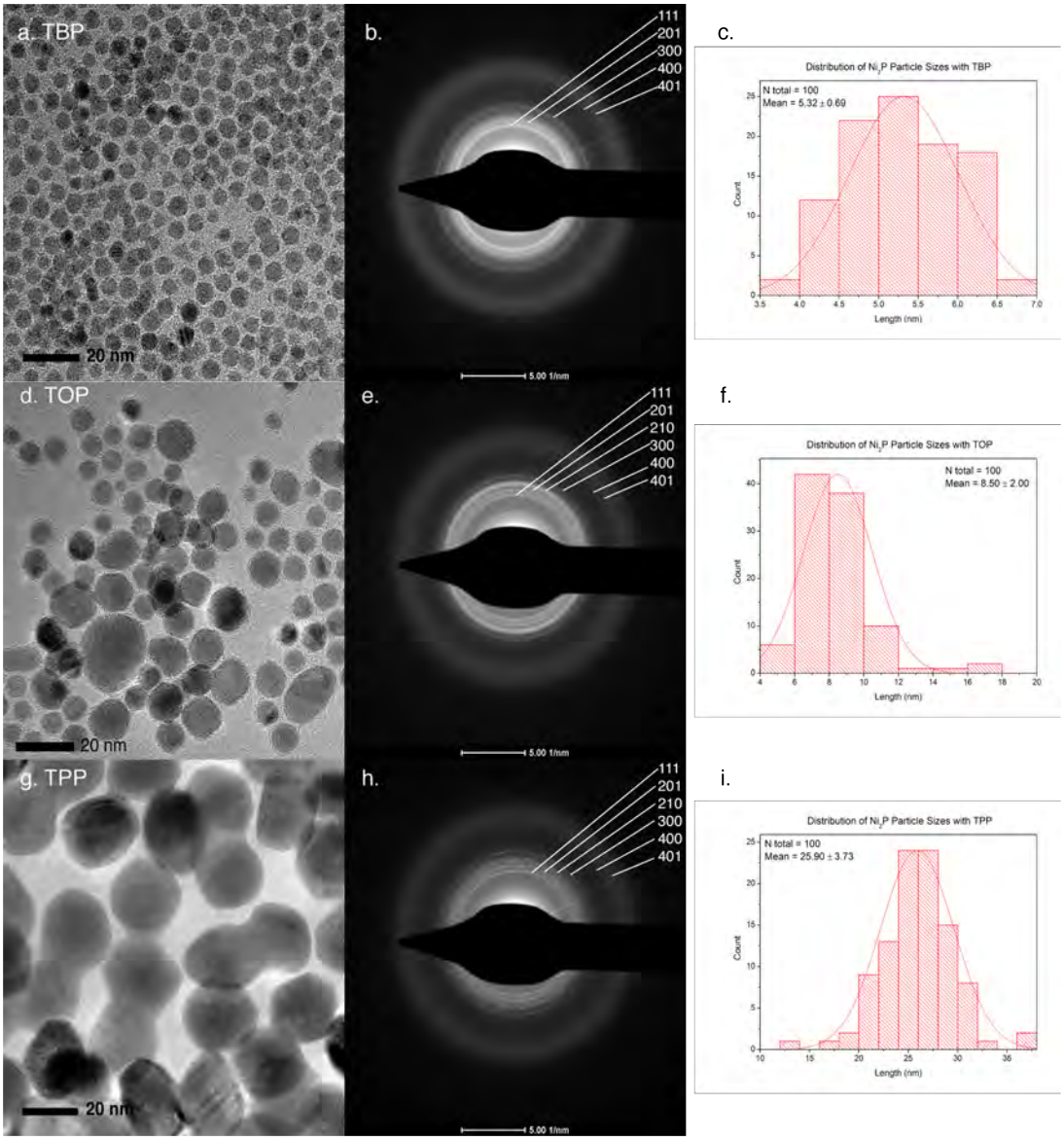

Figure 2.5. TEM, SAED (JCPDS no. 03-0953), and size distribution of Ni_2P when using tributylphosphine (TBP, a-c), trioctylphosphine (TOP, d-f), and triphenylphosphine (TPP, g-i) as ligands.

mass spectrometry (GC-MS) could be used to determine if the respective functional group of the ligands are present after the formation of the NPs. This could be done by running a sample of the supernatant after washing the NPs. If steric bulk were to be considered, shorter less sterically hindered ligands could react faster, forming smaller monodispersed NPs. The aryl functional group is more sterically hindering than the long and short chain alkyl group, which correlates directly with the NP sizes observed where TPP $>$ TOP $>$ TBP.

2.3.2 Surface Characterization of Ni_2P NPs with Phosphine Ligands

^{1}H NMR spectroscopy was used to identify the ligands present on the surface of the Ni_2P NPs. After washing and purifying the NPs, a small aliquot of the Ni_2P NPs was placed under vacuum to remove excess solvent and then analyzed in $CDCl_3$. In the spectra of TBP and TOP ligand standards (Figure 2.6b), the methyl and methylene protons are at 0.8 ppm and 1.2 ppm, respectively, where the protons of the phenyl groups in TPP are at 7.4 ppm. In analyzing the ^{1}H NMR spectra of the NPs, the presence of oleylamine is expected as it was involved in the reaction and traditionally acts as a surfactant in NP syntheses. A key feature of oleylamine is the double bond within the long alkyl chain, which gives rise to a unique peak at 5.3 ppm that corresponds to the vinyl protons (Figure 2.6b). The integration of the vinyl protons to the methyl in oleylamine is 2H:3H. In the spectra of Ni_2P synthesized with TBP ligands, the vinyl protons of oleylamine are present, but the 2H:3H integration is not seen. Instead, the integration of the vinyl protons to the methyl peak is 2H:6H, indicating that the extra methyl signal could be attributed to the methyls of the TBP ligands (Figure 2.6a). Due to the tumbling of NPs in solvent, the broadening of the NMR peaks or the depression of intensity can be attributed to the ligands bound to the surface of the NPs.

The ^{1}H NMR spectra of the Ni_2P NPs with TOP is quite similar to that of TBP, but with a vinyl to methyl integration of 2H:12H. The increase in methyl integration could pertain to the three methyls of the TOP ligand. As for the Ni_2P NPs with TPP, the strong singlet seen in the clean spectra of TPP has been suppressed, suggesting that TPP ligands are on the surface of the NPs. What is interesting was the integration of the vinyl and methyl protons, that should have been 2H:3H since there are no alkyls in TPP, was instead 2H:8H. The solvent may have not been completely removed during the washing of the NPs, or some type of ligand derivative left over from washing as well could be attributing to this increase in signal.

The next step was to perform a ligand exchange experiment in order to determine if the phosphine ligands are crystal-bound. Since crystal-bound ligands are resistant to ligand exchange, the respective NMR peaks of the phosphine ligands should remain, and the oleylamine and the exchanging ligands will be removed after the washing of the NPs.

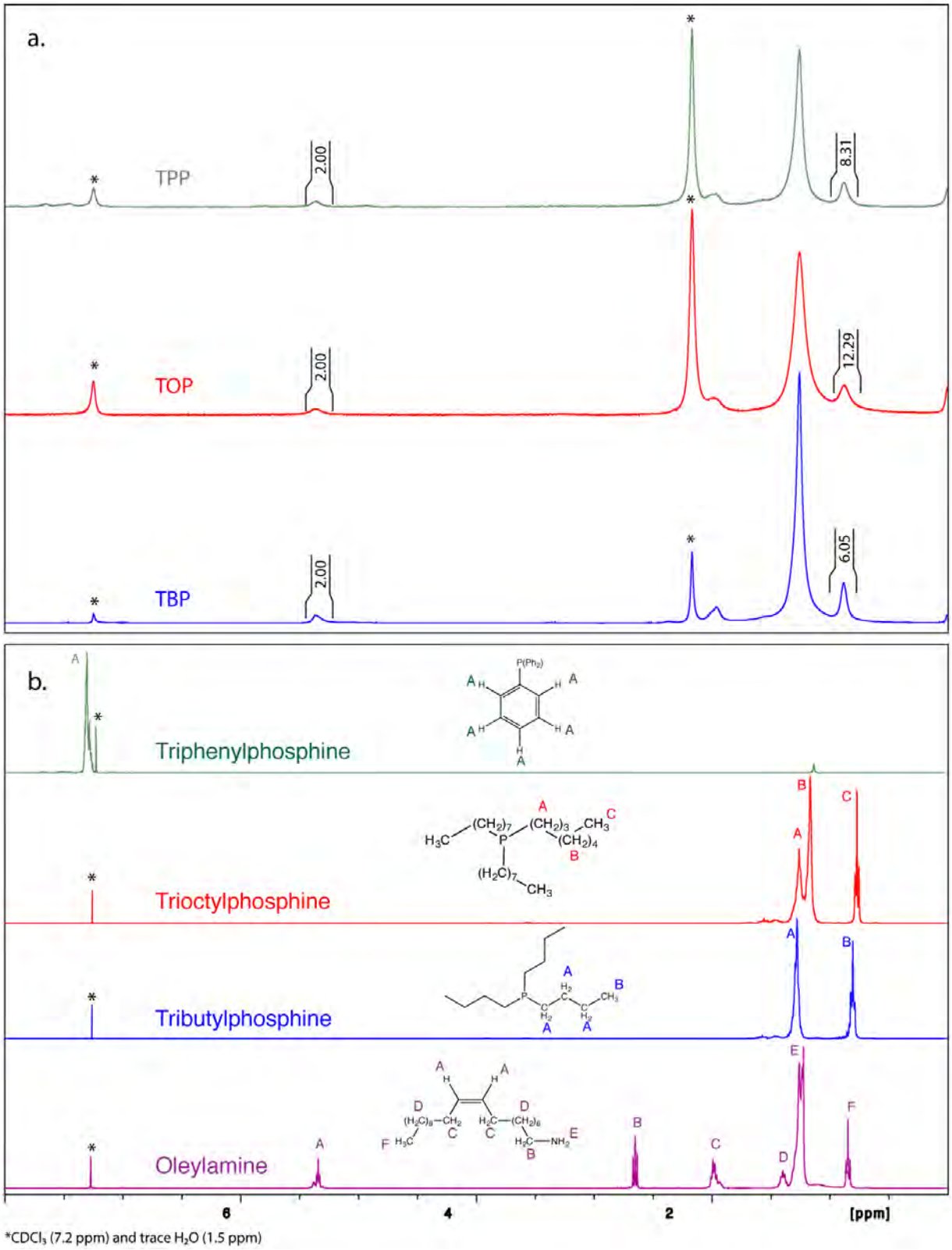

Figure 2.6. a.) ^{1}H NMR of Ni_2P synthesized in the presence of oleylamine and tributylphosphine (bottom), trioctylphosphine (middle), and triphenylphosphine (top). b.) ^{1}H NMR spectra of phosphine ligands (clean) and oleylamine.

During ligand exchange, another ligand with competitive capping ability displaces the current ligand on the surface. Amines (RNH_2) and phosphines (R_3P) are L-type ligands, which are Lewis bases, of neutral two-electron donors with a lone electron pair that datively coordinates surface metal atoms.[23,61] The exchange of NP surface ligands is similar to that of a substitution reactions in coordination complexes, which is highly dependent on solvent polarity and coordinating ability. L-type ligands rapidly adsorb and desorb from the surface at room temperature when in nonpolar solvents allowing for an L- to L-type ligand exchange to occur. TPP was used to displace the oleylamine and phosphine ligand on the NP surface as its peak appears in the aromatic region, making identification unambiguous. A 50 μL portion of the as-synthesized Ni_2P NPs was added drop-wise to a solution of 0.40 mmol TPP and chloroform. The mixture was stirred for 1 h in air, and then washed with acetone to remove an unbound ligands from the particles. If displacement is successful, signals correlating to phosphine ligands will be absent with TPP present in the aromatic region, which will indicate that the ligands are surface-bound. If displacement is unsuccessful, then the corresponding signals of phosphine ligands will remain, which will suggest that the ligands are crystal-bound.

The ^{1}H NMR spectra of Ni_2P prior to ligand exchange (Figure 2.7) all exhibit the characteristic peak at 5.3 ppm of the vinyl oleylamine protons, as well as the methyl and methylene peaks from the oleylamine and phosphine ligands (excluding TPP) at 0.8 and 1.2 ppm. After ligand exchange with TPP, the ^{1}H NMR of all three types of Ni_2P NPs revealed the absence of the double bond signal of oleylamine and a peak at 7.3 ppm characteristic of the protons of the phenyl groups on TPP. The presence of the phenyl peak in the samples where NPs had been prepared with TBP and TOP suggests that ligand exchange to TPP was successful. As for TPP, since the phosphine ligand is exchanging with itself, an increase in both peak sharpness and intensity was noticed due to the presence of free ligands. The broad peak around 1.5 and 2.2 ppm that appears after ligand exchange is trace water and residual acetone from the washing of the NPs. In all three samples after ligand exchange, is a very small signal at 1.3 ppm that likely results from the methylenes of either oleylamine or phosphine ligands that might still be on the surface of the NPs. More

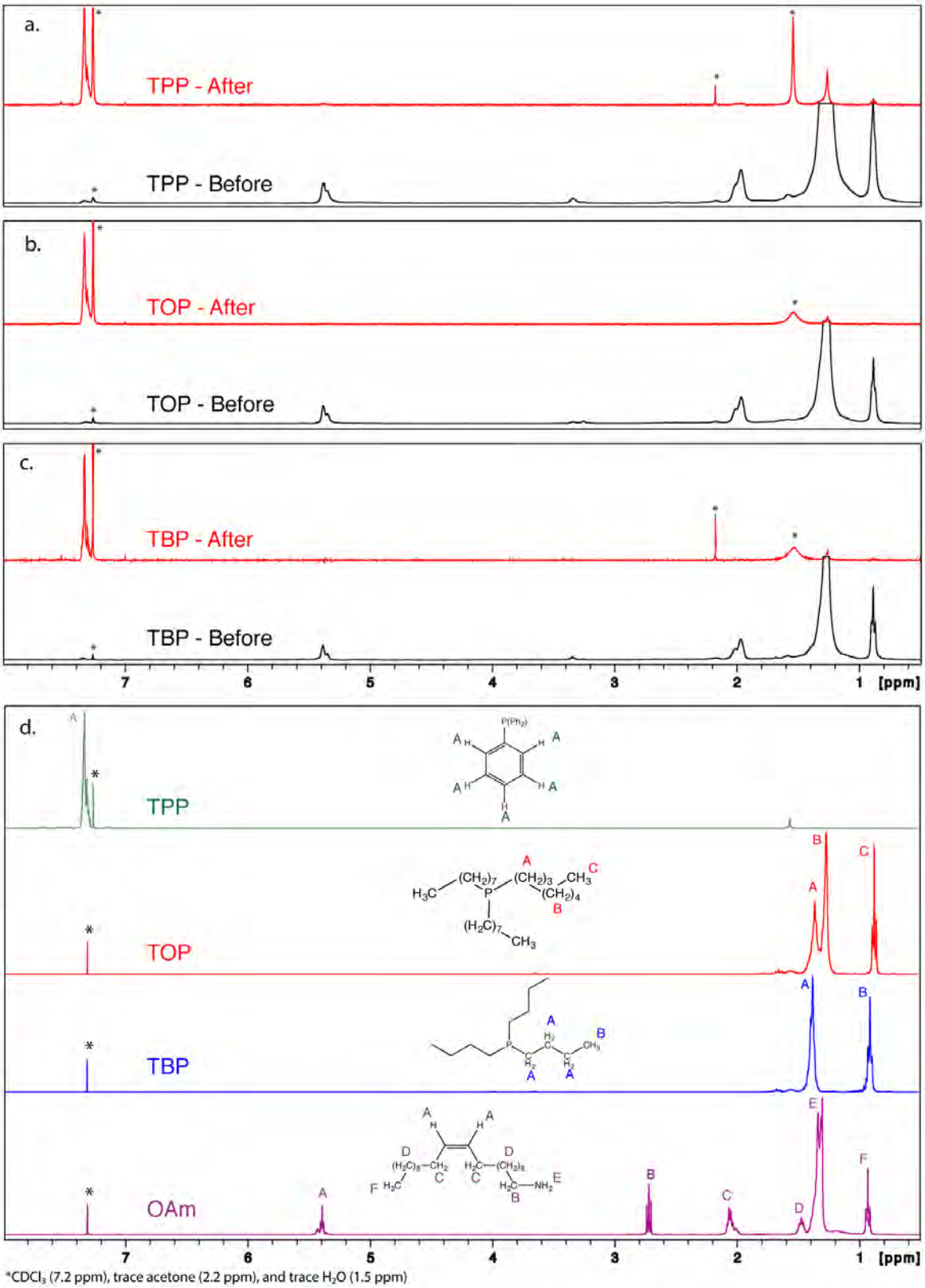

Figure 2.7. ^{1}H NMR of Ni_2P with a.) triphenylphosphine, b.) trioctylphosphine, and c.) tributylphosphine before (blue) and after (red) ligand exchange with triphenylphosphine. d.) ^{1}H NMR spectra of phosphine ligands (clean) and oleylamine.

studies are needed for further validation of the ligands present and their respective binding modes, such as Fourier transform infrared spectroscopy (FT-IR) taken before and after ligand exchange.

What is clear from this ligand exchange experiment is that oleylamine acts as an important ligand for the Ni_2P NPs synthesized with TBP, TOP, and TPP. While there may also be some phosphine ligands on the surfaces after synthesis, since ligand exchange appears facile, the binding mode of any phosphine ligands are not likely to be crystal-bound; our previous studies with crystal-bound thiols on Cu_2S showed that this binding mode is highly resistant to ligand exchange. There is also a high probability that crystal-bound ligands cannot be achieved at the reaction temperature of 320°C as it is causing very facile P–C cleavage of the ligands. This supports the difference in Ni_2P NPs sizes synthesized with TBP and TOP and TPP, as TPP phenyl groups will have a stronger P–C bond than the alkyl groups on TBP and TOP. This results to an increase in size because there are not enough ligands available to decrease the surface energy of the NPs, which allows growth of the NPs to continue.

Possible studies in validating the phosphine ligand binding mode on the surface of the Ni_2P NPs include thermogravimetric analysis mass spectrometry (TGA-MS) and X-ray photoelectron spectroscopy (XPS). TGA-MS is a technique that tracks mass loss as a function of time, making it possible to determine the coordination of the phosphine ligand on the surface. If the phosphine ligand is surface-bound, the phosphines will be left in low coordination sites where they can be easily removed at higher temperatures. This should not be the case with crystal-bound NPs, as the phosphine ligands sit in higher coordination sites, preventing mass loss.[27] XPS can also reveal information about the surface chemistry of NPs as it can reveal the difference between crystal-bound and surface-bound ligands, where surface-bound ligands may be similar to the phosphorus binding energies in the XPS spectra of bulk Ni_2P.[30] These two studies will help conclude the surface chemistry of the phosphine ligands in the synthesis of Ni_2P, which could later lead into the optimization of its synthesis for further control for modifying the surface chemistry.

2.3.3 The Effects of Temperature on the Composition of Ni_2P NPs

The growth of colloidal NPs is highly dependent on the precursor concentration, the reactivity of the ligand, and the reaction temperature which may all lead to alternative surface chemistries. So far, the reactivity of the ligands only affected the size of the Ni_2P NPs, where the morphology, composition, and structure was unaffected. A successful ligand exchange experiment performed in section 2.3.2 insinuated that crystal-bound ligands can not be achieved at the reaction temperature of 320°C, independent to the type of phosphine ligand used. In this section, the effect of temperature on the growth and surface chemistry of Ni_2P NPs is examined. There is the possibility that the P–C bonds of the phosphine ligands are cleaving too easily at 320°C. By decreasing the temperature, it is hypothesized that the P–C cleaving of the phosphine ligands will be impeded, allowing the phosphine ligands to become crystal-bound. A balance must be achieved; the temperature must be high enough such that P–C bonds are cleaved to allow the formation of Ni_2P, but low enough that the P–C cleavage is limited in some way such that crystal-bound ligands on the surface are achieved. Similarly, our research group found that crystal-bound ligands are resistant to ligand exchange of thiols on CdSe@ZnS (reaction temperatures of 200°C), but the Bawendi Group using similar conditions, but higher temperatures (310°C) found no-such impairment of ligand exchange.[62]

TOP was chosen for this study as it is an ideal ligand that may result in crystal-bound ligands as it can function as an anion source, coordinating ligand, and NP stabilizer. TOP could eventually replace the need of oleylamine in the reaction if a crystal-bound binding mode of ligands can be achieved. The reaction temperature for the organometallic decomposition reaction ranged from 265–300°C. The resulting NPs were compared to Ni_2P NPs with TOP previously synthesized at 320°C. Before evaluating if the temperature changes the surface chemistry of the NPs via ^{1}H NMR, the morphology was characterized along with the composition and crystal structure.

TEM images of the Ni_2P NPs throughout the temperature range show that there was not a significant change in morphology compared to the Ni_2P NPs made at 320°C (Figure 2.8). Semi-pseudo-spherical NPs were formed with subtle differences in monodispersity and size. At the

low temperatures of 265°C and 275°C, the NPs were very polydispersed and larger in size than the Ni_2P NPs synthesized at 320°C (13.9 ± 3.6 nm, 14 ± 2.9 nm respectively). Interestingly, a shell can be observed around the NPs at 275°C. At temperatures of 285°C and above (Figure 2.8c-f), a shift in shape uniformity and monodispersityis observed, as well as a steady decrease in size from 13.5 ± 1.5 nm (285°C) to 8.5 ± 2.0 nm. Occasionally hollow NPs were observed due to the prominent Kirkendall effect that occurs in the synthesis of Ni_2P.[55] When comparing the morphology of the NPs synthesized from 285–300°C to the NPs synthesized at 320°C, the standard deviation is smaller at the lower reaction temperatures, suggesting that uniform growth could be occurring at these temperatures, or that coalescence may be increasing at the extreme temperature of 320°C.[8] This is the opposite of the trend that Habas *et.al.* described, where they reported an increase in NP size from 10–16 nm from temperatures 275–320°C, and then a decrease of size to 14 nm after aging for 2 h.

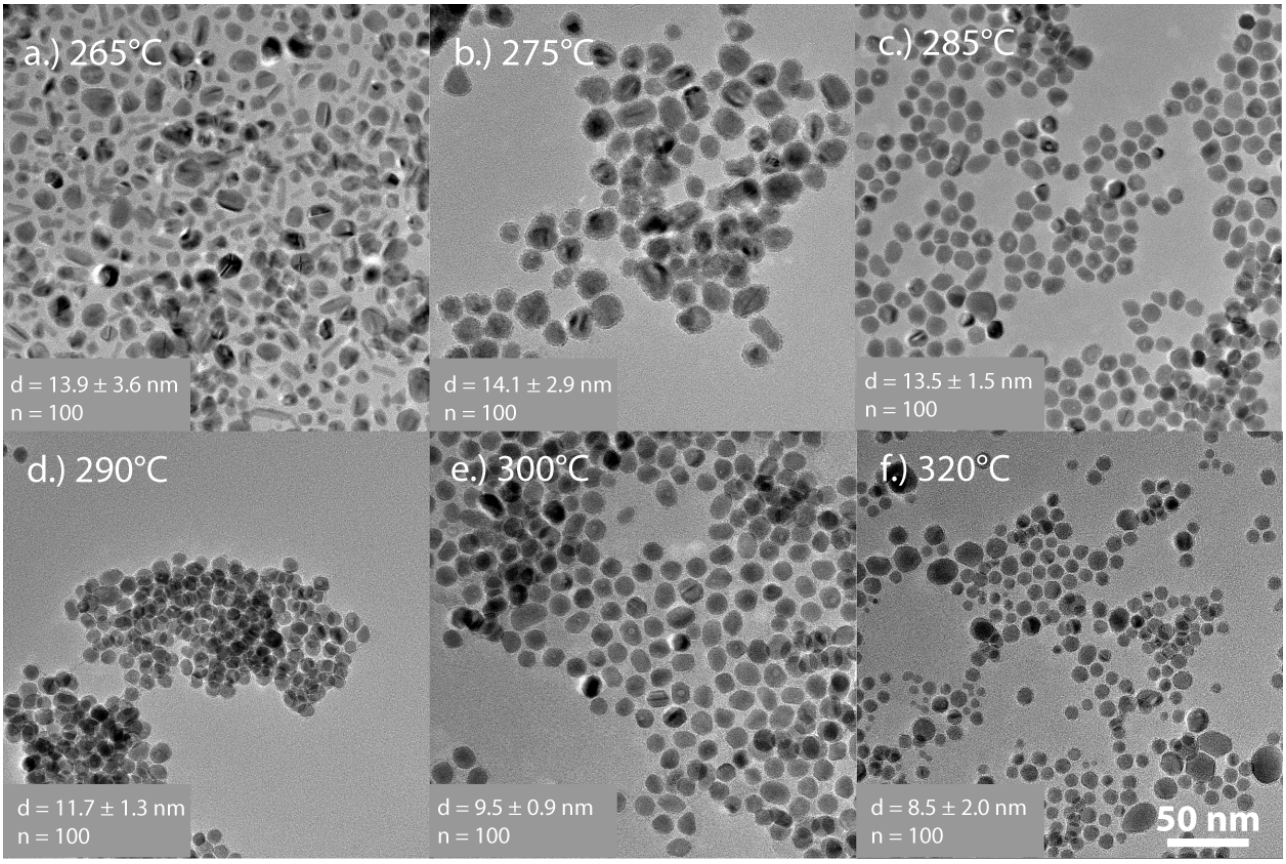

Figure 2.8. TEM images of Ni_2P NPs prepared at reaction temperatures from 265–320°C (a.-f.).

The EDS map collected from the samples prepared from 265–320°C uncovered a mechanism of formation of the Ni_2P NPs that was more complicated than what was previously reported by the Habas group. Figure 2.9 shows clusters of P atoms surrounding Ni seeds. At 265°C (a.), where the SAED pattern (Figure 2.10a) supports cubic Ni present. The quantification of Ni/P content in the EDS map resulted in a Ni to P stoichiometric ratio of 5:1 (Table 2.1).

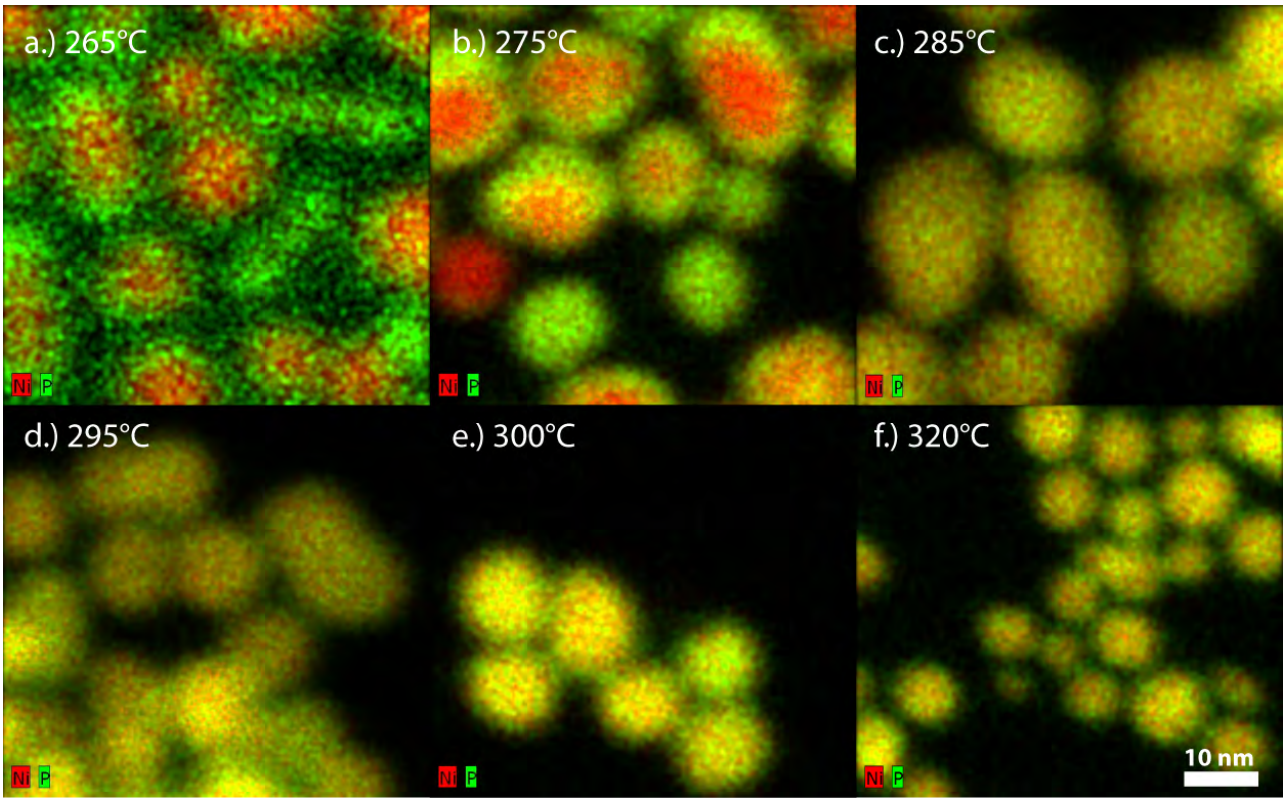

Figure 2.9. EDS map of Ni_2P NPs prepared at reaction temperatures from 265–320°C (a.-f.).

As the temperature increases to 275°C, core-shell NP formation is observed (Figure 2.9b). This 10°C increase adds enough energy into the system for the P–C bond to cleave, where P atoms begin to intercalate into the surface of the Ni seeds resulting in core-shell NPs. There are two phases present at 275°C (Figure 2.10b): a cubic Ni core and hexagonal close packed Ni_5P_2 shell. At 285°C and 295°C there is complete intercalation of P atoms into the Ni seeds (Figure 2.9c-d), supported by the Ni phase no longer being present. Ni_5P_2 is still present, but the structure continues to shift as more P atoms enters the NPs. Tetragonal $Ni_{12}P_5$ and hexagonal Ni_2P phases now exist, resulting in a total of three phases present in the NPs at these temperatures (Figure 2.10c-d). The

NPs at 285°C and 295°C have a Ni to P ratios of about 2:1 (Table 2.1) Once the temperature reaches 300°C, the structure has shifted once again and Ni_5P_2 is no longer present, but the same compositional uniformity remains with a Ni to P ratio of 2:1 (Figure 2.9e). The NPs at 300°C comprise both tetragonal $Ni_{12}P_5$ and hexagonal Ni_2P (Figure 2.10e). It is not until the temperature reaches 320°C that pure Ni_2P phase is observed (Figure 2.10f).

Table 2.1. Temperature Effect on the Composition of Ni_2P with TOP

Temperature	*Atomic Ratio*	
$(°C)$	*Ni*	*P*
265	4.8	1
275	5.2	1
285	2.2	1
290	2.1	1
300	2.1	1
320	1.7	1

The mechanism of formation of Ni_2P NPs was made evident through the EDS maps collected. Thermal decomposition of the Ni carbonyl compound at 265°C leads to the nucleation of Ni seeds. At 275°C, the temperature is high enough to cause P–C bond cleavage of the TOP ligands, beginning the diffusion of P atoms into the Ni seeds. At 285°C diffusion is complete, the percent of P atoms reaches a saturation point as it is maintained between 28–29% from 285–320°C. The NPs go through intermediate Ni_xP_y phases as temperature increases until pure Ni_2P is reached at 320°C. The XRD patterns of Ni_xP_y NPs at each temperature provides a visual representation of the mechanism of formation, where multiple shifts in structure are observed until pure Ni_2P is reached (Figure 2.11a).

The last feature observed was the effect the TOP ligands have on the stability of the NPs via UV-Vis spectroscopy (Figure 2.11b). When the NPs were primarily composed of Ni at 265 and 275°C, featureless absorbance is observed as a result of scattering. At the temperature of 285°C, a

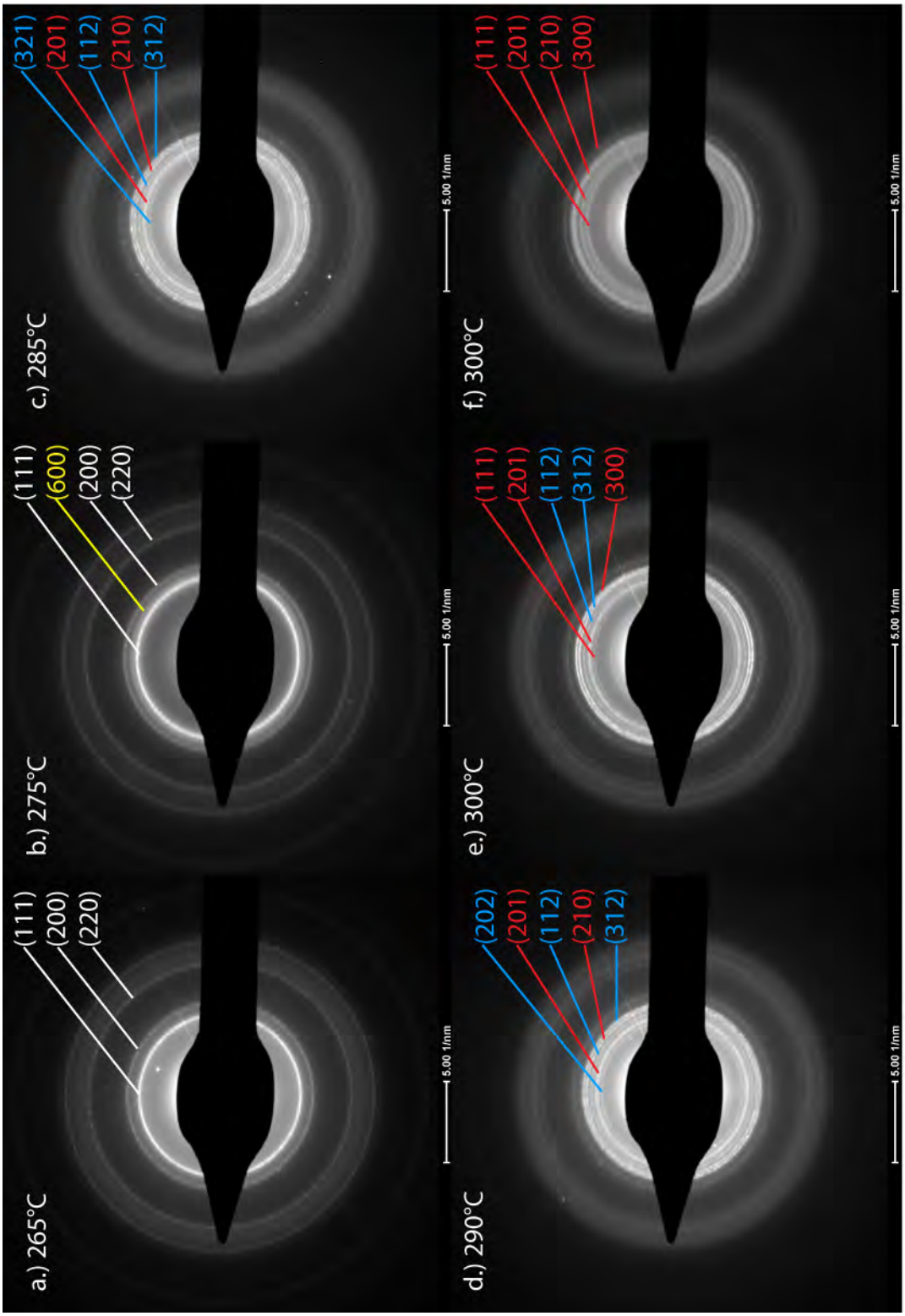

Figure 2.10. SAED patterns of Ni_2P NPs prepared at reaction temperatures from 265–320°C (a.-f.). *KEY: white = cubic Ni (JCPDS no. 03-1051), yellow = hexagonal Ni_5P_2 (JCPDS no. 17-0225), blue = tetragonal $Ni_{12}P_5$ (JCPDS no. 22-1190), and red = hexagonal Ni_2P (JCPDS no. 03-0953).*

typical absorbance spectra of NPs becomes apparent and decreases as temperature increases. The decrease in absorbance could correlate to the NP size decreasing as temperature increases due to the availability of TOP ligands decreasing as a result of P–C bond cleavage.

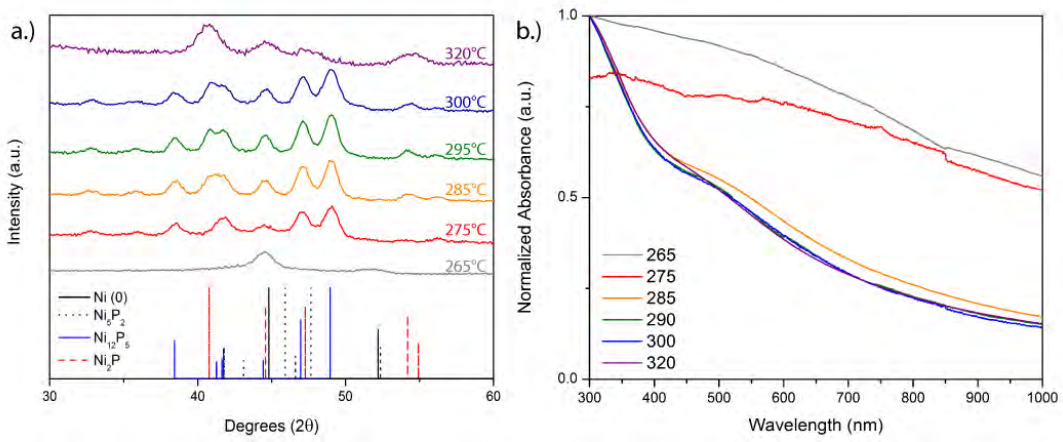

Figure 2.11. a.) XRD patterns and b.) UV-Vis absorbance spectra of Ni_2P NPs prepared at reaction temperatures from 265–320°C. Data for Ni, Ni_5P_2, $Ni_{12}P_5$, and Ni_2P are from JCPDS cards no. 03-1051, 17-0225, 22-1190, and 03-0953, respectively.

2.3.4 The Effects of Temperature on the Surface of Ni_2P NPs

As the reaction temperature of the Ni_2P NPs decreases, TOP ligands are expected to become crystal-bound as P–C bond cleavage is likely happening at a slower rate. The ^{1}H NMR spectra of the Ni_2P NPs synthesized at the reaction temperature of 265–320°C are shown in Figure 2.12. The vinyl proton signal of the double bond in oleylamine is present at 5.3 ppm from 320°C to 285°C. The sharp appearance of that peak at 320°C suggests that there is free oleylamine and not tightly bound to the surface of the NPs. The double bond peak becomes broader with respect to the 320°C as the temperature decreases to 285°C. This could be attributed to NPs being smaller and the oleylamine binding more tightly to the NPs.[63] Due to the NPs being mostly comprised of metallic Ni at 265 and 275°C, the NPs interfere with the magnetic field of the ^{1}H NMR.

It is possible to determine the ratio of ligands present on the surface of the NPs through the NMR integrations, as the integration at 0.8 ppm pertains to the methyl group in both oleylamine (OAm) and TOP using equation 2.1.

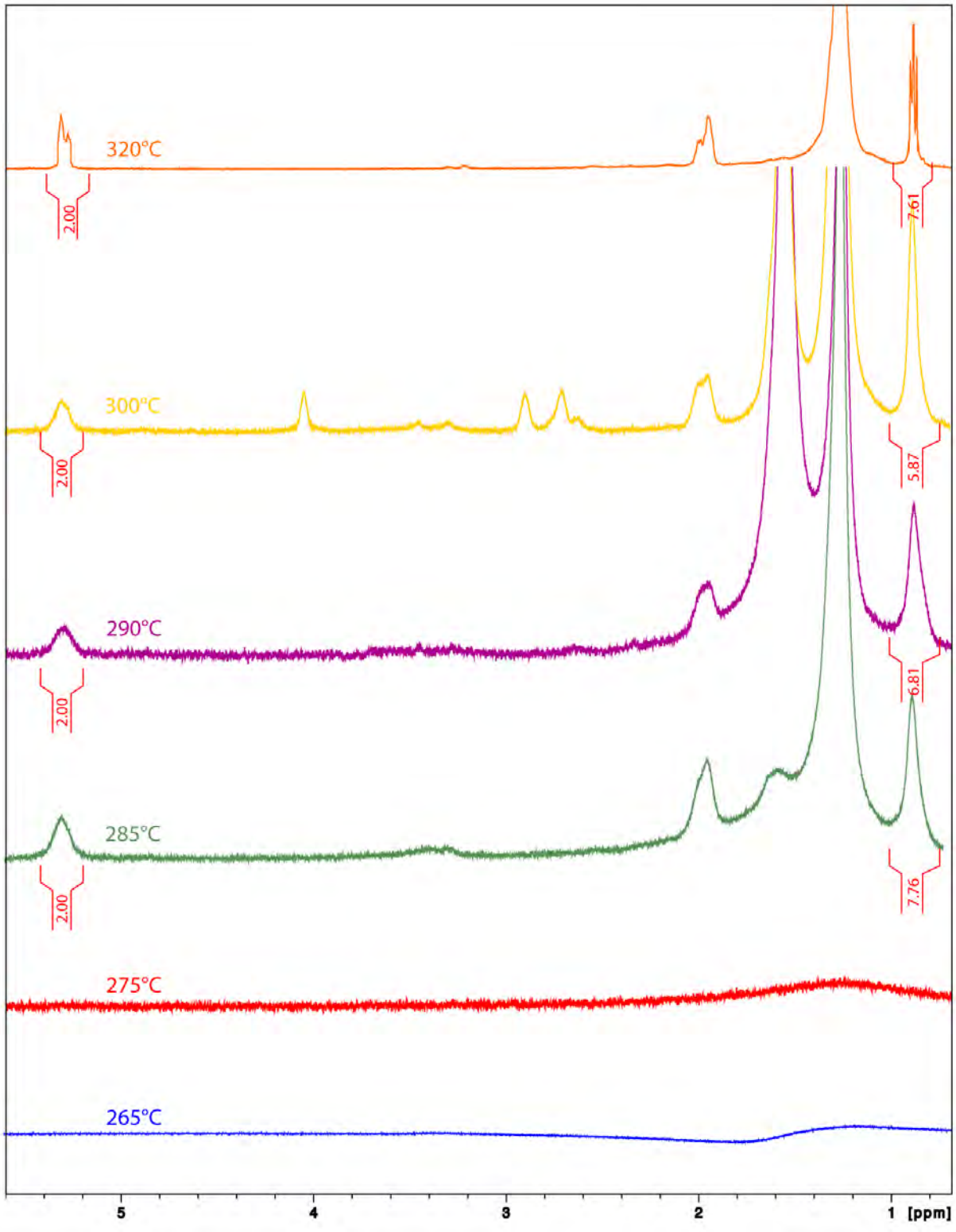

Figure 2.12. ^{1}H NMR spectra of Ni_2P NPs prepared at reaction temperatures of 265 – 320°C.

$$CH_3^{int} = CH_3^{OAm} + CH_3^{TOP} \tag{2.1}$$

Equation 2.1 can be rearranged to solve for the number of TOP molecules present on the surface. The vinyl protons of oleylamine at 5.3 ppm was calibrated to have an integration of 2.00 (Figure 2.12). Per one oleylamine molecule, there is one methyl group. Now there are two knowns in equation 2.1, and the number of TOP molecules can be determined.

$$CH_3^{TOP} = CH_3^{int} - CH_3^{OAm} \tag{2.2}$$

$$CH_3^{TOP} = CH_3^{int} - 3.00 \tag{2.3}$$

However, there are three methyl groups per one TOP molecule, totaling 9H that must be accounted for. Equation 2.3 becomes

$$CH_3^{TOP} = \frac{CH_3^{int} - 3.00}{9} = number\ of\ TOP\ molecules \tag{2.4}$$

where the ratio of oleylamine to TOP molecules was determined by dividing the number of TOP molecules by 1 oleylamine molecule, resulting in 1.89, 2.36, and 3.14 as the reaction temperature increased from 285–300°C (Table 2.2). As less phosphine ligands become available, oleylamine becomes the predominant surface ligand to maintain low surface energy and provide colloidal stability. There is a slight decrease in the oleylamine/TOP ratio at 320°C to 1.95, which may be a result of there being less oleylamine on the surface, as the NMR spectra shows there is free oleylamine present.

Table 2.2. Temperature Effects on the Surface of Ni_2P with TOP

Temperature (°*C*)	265	275	285	290	300	320
OAm to TOP	–	–	1.89	2.36	3.14	1.95

2.4 Conclusion

The surface chemistry of Ni_2P NPs was determined via a thermal decomposition reaction of $[Ni(CO)_2(PPh_3)_2]$ and ^1H NMR techniques. The effect of using three different phosphine ligands in an effort to induce the crystal-binding of the phosphine ligands in the Ni_2P NPs was evaluated. Prior to examining the Ni_2P NPs surfaces, the morphology, size, structure, and composition were characterized via TEM, SAED, and EDS. All three phosphine ligands resulted in pseudo-spherical pure phase Ni_2P NPs at the reaction temperature of 320°C. The use of TBP, TOP, and TPP ligands led to an increase in NP size, which could be related to the P–C bond strength or the steric effects of the ligands. P–C bond strength of the phosphine ligands increase from TBP $<$ TOP $<$ TPP, where the probability of cleavage decreases, leading to an increase in NP size. The bulkiness of the phosphine ligands increase from TBP $<$ TOP $<$ TPP, where TPP is more sterically hindering, subsequentually producing the largest distribution of NPs when compared to NPs with TBP and TOP. The ^1H NMR spectra of the Ni_2P NPs with TBP, TOP, and TPP revealed that there are phosphine ligands present on the surface of the NPs along with oleylamine. A successful ligand exchange of all three types of NPs with TPP suggests that none of these phosphine ligands was crystal-bound.

One explanation for the lack of crystal-binding is that the thermal decomposition reaction temperature may have been too high, favoring the P–C cleavage of phosphine ligands. The reaction temperature was studied to see if crystal-bound ligands can be accessed at the lower temperatures of 265–320°C. TOP was chosen for this study because it is an ideal ligand to function as a crystal-bound ligand, as it can be the anion source, coordinating ligand, and NP stabilizer. The resulting NPs synthesized at each temperature produced pseudo-spherical morphologies similar to the Ni_2P NPs made at 320°C. Although there was a shift in the distribution of size as temperature increased, SAED and EDS revealed that the mechanism of formation of the Ni_2P NPs may in fact be more complicated than what Habas *et. al.* reported. As temperature increases, there is a shift from cubic Ni seeds at 265°C to core-shell NPs of Ni and hexagonal Ni_5P_2 at 275°C. At this temperature, phosphidation begins as a result of the P–C bond cleavage in TOP. At 285°C to 300°C, there

is complete saturation of P atoms, and EDS shows that P content plateaus at 285°C. There is a constant shift in structure where hexagonal Ni_5P_2, $Ni_{12}P_5$, and Ni_2P are present from 285–300°C, eventually reaching pure phase Ni_2P at 320°C. XRD patterns of the Ni_xP_y NPs further supported the EDS map data, and the new proposed mechanism of formation is depicted in Figure 2.13.

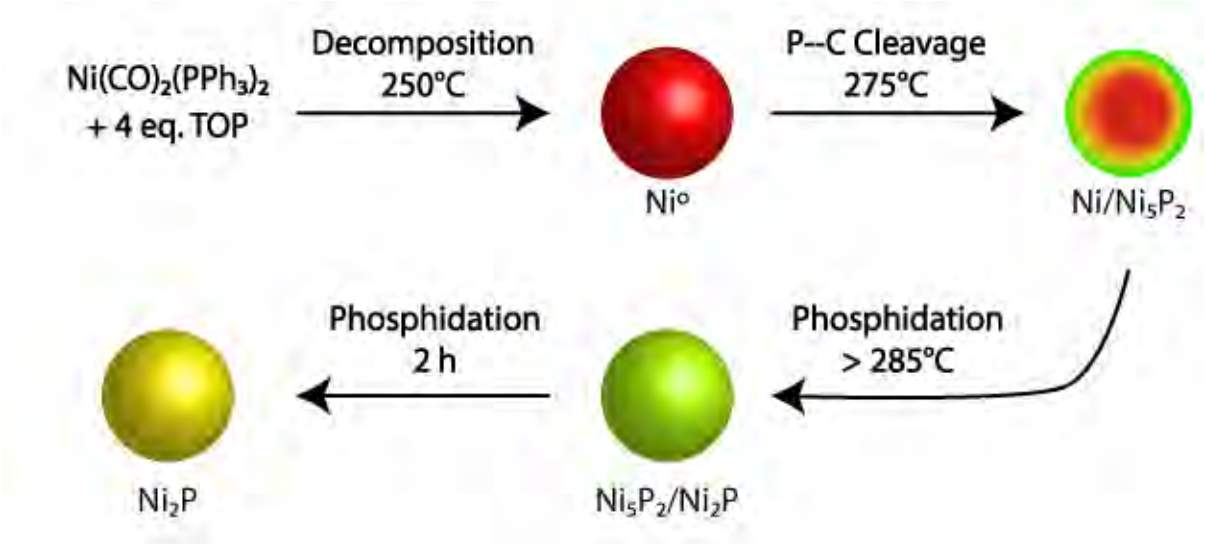

Figure 2.13. Illustration of new mechanism of Ni_2P NPs formation based on temperature dependent study.

Through the integration of the vinyl protons of oleylamine and the methyl protons of oleylamine and TOP in the ^1H NMR spectra of the NPs synthesized at each reaction temperature, the ratio of oleylamine to TOP molecules on the surface was determined. When the diffusion of P atoms into the Ni seeds reached saturation, more oleylamine ligands appeared on the surface of the NPs. The NPs formed at 275°C are more likely to have a greater amount of TOP molecules on the surface, as P–C cleavage appears to be occurring at a slower rate than at 285°C and above. The Ni core of the NPs is metallic by nature and interferes with the magnetic field of the NMR. This is unfortunate, as there is a greater potential for the TOP ligands to be crystal bound at this reaction temperature. Ligand exchange studies could be done along with FT-IR and TGA-MS to conclude the binding mode of the TOP ligands.

Overall, the work described in this chapter concludes that the diffusion of P atoms is limited by the cleavage of the P–C bond. There are some discrepancies from the mechanism of Ni_2P

NPs in literature, but this can be attributed to the reaction conditions. The nucleation of Ni seeds seen at 265°C is similar to what was seen when nickel (II) acetylacetone or acetate was used as the metal precursor in the presence of oleylamine and TOP.[55,64] When a nickel salt is in the presence of TOP alone, the formation of Ni_2P NPs also went through Ni seeds.[65,66]. Nickel (II) acetylacetonate or acetate led to the formation of hollow Ni_2P NPs at the reaction temperature of 330°C. The nickel carbonyl compound, $[Ni(CO)_2(PPh_3)_2]$, used in this study has two TPP ligands within its complex that contribute to the reaction, increasing the P content and causing solid Ni_2P NPs to be produced instead. The studies that observed the nucleation of Ni seeds did not report a mechanism of formation including other intermediate phases prior to Ni_2P. This is the first time the intermediate phases have been isolated, where an increase of temperature from 275 to 320°C leads to solid, pure phase Ni_2P NPs with TOP.

Simplification of the thermal decomposition reaction of Ni_2P could aid in identifying the surface chemistry of the Ni_2P NPs surfaces. Oleylamine competes with phosphine ligands, as they are both L-type ligands. By removing oleylamine and octadecene from the system and using TOP in place of the solvent, NP stabilizer, and coordinating ligand, it would be possible to form crystal-bound ligands. The disadvantage of this is that P–C cleavage of the ligand is required in order for phosphidation to occur. However, if there is excess TOP when diffusion reaches saturation, there is still a chance the surface P atoms will have their ligands intact and become crystal-bound. If crystal-bound Ni_2P nanoparticles can be obtained, the use of a support would not be needed, as crystal-bound ligands increase stability and robustness, as well as increase the number of available metal atoms on the surface, increasing catalytic activity. Other techniques such as FT-IR, TGA-MS, and XPS can be used in conjunction with ^1H NMR for a detailed surface characterization of Ni_2P NPs. This study could aid in the optimization of current Ni_2P NPs for use as a heterogeneous catalyst for water splitting, water oxidation, hydrogen evolution, hydrodeoxygenation, and hydrodesulfurization processes. It is important to understand the surface chemistry of nanomaterials for proper functionalization and application.

CHAPTER 3

AN INVESTIGATION OF COBALT SULFIDE NANOPARTICLES FOR HYDROGEN EVOLUTION PROCESSES

3.1 Project Idea of Cobalt Sulfide Particles as Electrocatalysts

Pt and Pt-based materials are the most efficient electrocatalysts due to their high current density and low onset potential, but their high costs and scarcity drives research for alternative electrocatalytic materials. A number of earth abundant, transition metal chalcogenides that exhibit high catalytic activity, scalability, and low cost have emerged in the form of amorphous NPs that renders them attractive candidates to replace Pt in electrocatalytic processes. Cobalt sulfide, a transition metal chalcogenide, is a II-VI semiconductor material that has been used for optical sensors, optoelectronic devices, magnetic devices, lithium ion batteries,[67] and as catalysts. Similar to Ni_2P, cobalt sulfide NPs can be used as heterogeneous catalysts for hydrodesulfurization,[68,69] but there is more potential for cobalt sulfide materials to be used as electrocatalysts for oxygen evolution/reduction and hydrogen evolution reactions.[70–72]

Cobalt sulfide NPs have been prepared using various methods such as hydrothemal, solvothermal, microwave-assisted, and thermal decomposition methods.[73,74] The challenge for shape controlled synthesis of cobalt sulfide NPs is caused by the vast range of stoichiometries of cobalt sulfides, which includes Co_4S_3, Co_9S_8, CoS, $Co_{1-x}S$, Co_3S_4, Co_2S_3, and CoS_2. Due to the variety of stoichiometries that cobalt sulfide can exhibit, current studies of cobalt sulfides are focused on exploiting the phase and morphology; controlling their morphology is critical, as most of the cobalt sulfide NPs have been amorphous.[69,70,73,75,76] Again, like the studies of Ni_2P, their surfaces have not been characterized before their electrocatalytic activity is tested, which should be a complimentary study as most heterogeneous processes are surface-dependent.

In this chapter, cobalt sulfide is synthesized via a solvothermal method in which cobalt (II) acetylacetonate hydrate ($Co(acac)_2$) is the metal precursor and dioctylether is the non-coordinating

solvent. Primary sulfide ligands have already been shown to successfully form crystal-bound NPs; a modification of Robinson *et. al.* solvothermal syntheses of crystal-bound Cu_2S NPs was utilized.[27,60] The goal is to form Co_2S NPs where the primary thiol ligands used are crystal-bound. Three primary aryl thiol ligands are used to determine the effect the ligands have towards the morphology and surface of the cobalt sulfide NPs. It is also expected that having a crystal-bound system may result to higher catalytic activity compared to particles that are surface-bound, as more active metal sites would be available on the surface of the NPs. NMR as well as Fourier transform infrared spectroscopy (FT-IR) spectroscopy will provide knowledge of the ligands present on the surface. The hydrogen evolution reaction (HER) activity of the as synthesized cobalt sulfide NPs will be tested utilizing linear sweep voltammetry (LSV).

3.2 Preliminary Results & Discussion

3.2.1 Synthesis of Cobalt Sulfide NPs

A procedure based on the solvothermal synthesis of crystal-bound Cu_2S NPs reported by Robinson *et. al.* was modified to produce cobalt sulfide NPs.[60] Complete experimental details can be found in Appendix A.1. Briefly, cobalt(II) acetylacetonate hydrate and an aryl thiol ligand were heated to 200°C in dioctylether, and stirred for 1 h. The aryl ligands used consist of a parent benzyl thiol structure where their differences arise from the substitutional group located at the para position. The substitutional groups are methyl (Me), *tert*-butyl (t-Bu), and trifluoromethyl (CF_3), depicted in Figure 3.1, and increase in electronegativity. It is expected that fairly large particles would form, as seen in Ni_2P NPs when tributylphosphine ligands were used, since the bulky aryl thiol slows down the kinetics of growth due to steric effects. The substitutional groups should have an effect on the kinetics of growth; in particular, the more electronegative CF_3 group should increase reactivity. Yet the bulky t-Bu and CF_3 substituents have the potential of blocking the metal sites on the surface of the NPs, and may lead to the decrease of catalytic activity. Before evaluating the effect the ligands have on the electrochemistry, the morphology and surface character were first

established.

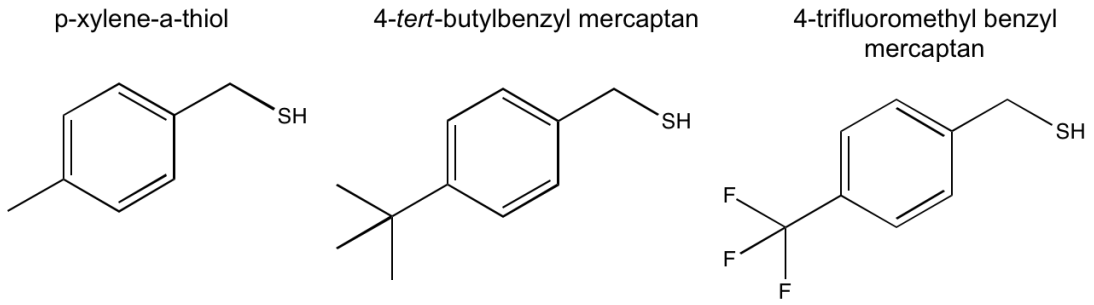

Figure 3.1. Primary thiols ligands used in the solvothermal synthesis of cobalt sulfide.

3.2.2 Morphology and Composition of Cobalt Sulfide Particles

The t-Bu ligands were used as the basis in establishing the parameters of the synthesis. In the Turo *et. al.* studies, the importance of temperature was reported, where crystal-bound NPs occur in a narrow temperature range spreading only 5°C. $Co(acac)_2$ in the presence of t-Bu ligands was used to produce cobalt sulfide particles in the temperature range from 80–200°C. TEM was used to determine morphology, and SAED and EDS were used to determine structure and elemental composition. There is a lack of defined morphology, as seen in Figure 3.2, as the temperature of reaction decreased from 200 to 80°C resulting in amorphous particles that are greater than 100 nm. At 200°C, it appears as if numerous NPs agglomerated together to form larger NPs. One cause of the amorphous structure at this temperature is the fact that the reaction is occurring well above the boiling point of the t-Bu ligands (103°C).

Looking at the EDS, the surface of the cobalt sulfide has begun to oxidize or begin to intercalate into the system as cobalt ions have a very strong affinity for oxygen. At 145°C, there seems to be cobalt oxide particles within some type of sulfide film/layer. The reaction temperature is still well above the boiling point of the ligand, and the product could be a result of S–C cleavage. At 100°C, large amorphous cobalt sulfide particles are present and surrounded by small nuclei of either cobalt sulfide or cobalt oxide NPs. The EDS shows that oxygen atoms are dispersed within the structures and are not localized on the surface of the particles. At 90°C, the nuclei previously mentioned are no longer present and there is somewhat a more compact morphology. The EDS indicates that there

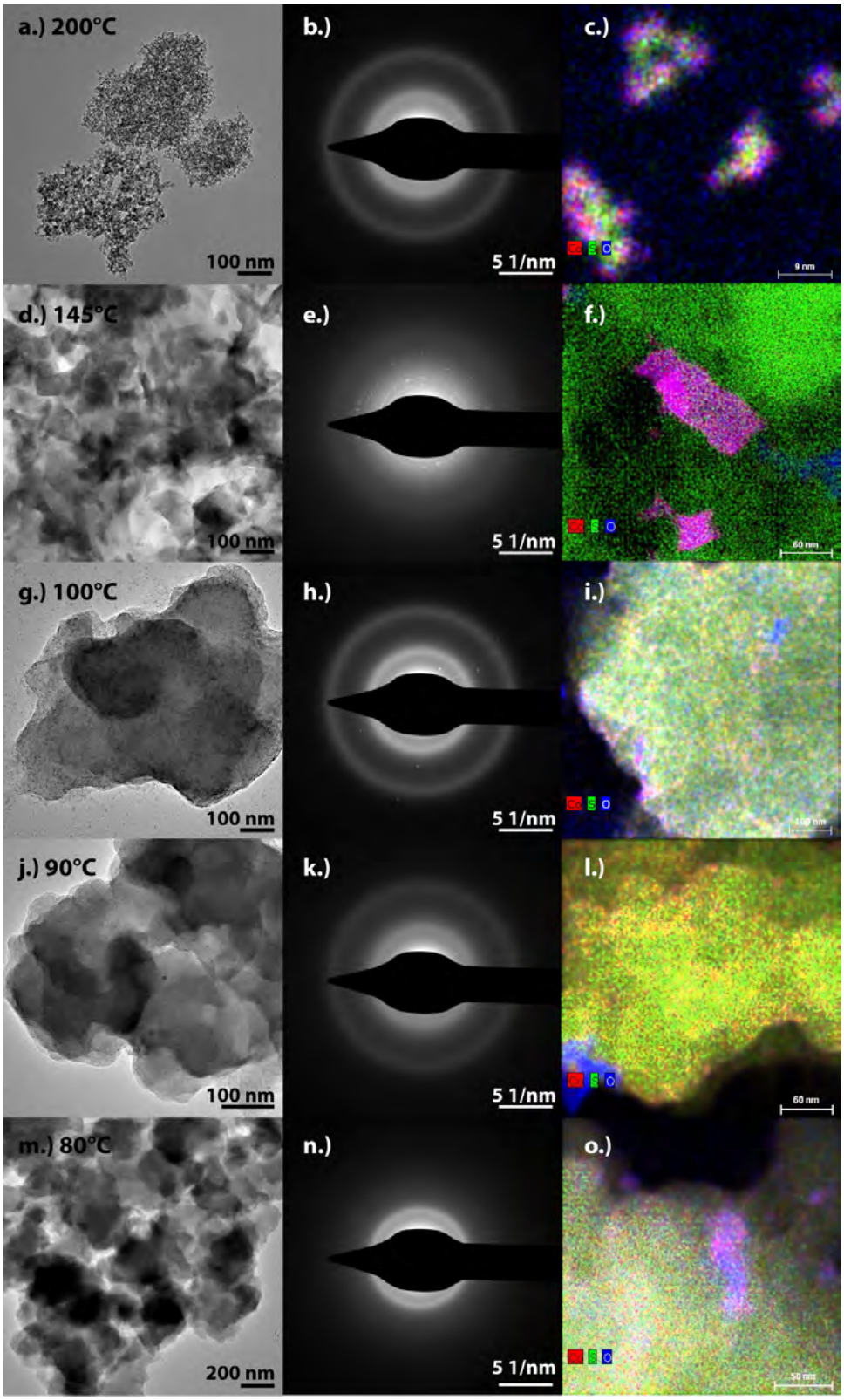

Figure 3.2. TEM, SAED, and EDS of cobalt sulfide particles synthesized with 4-*tert*-butylbenzyl mercaptan ligands.

is predominately cobalt sulfide with fewer oxygen atoms present compared with the previous temperatures. At 80°C oxygen atoms are present within the particles, which appear to be more compact than the particles at 90°C. The reaction temperatures of 80–200°C resulted in amorphous particles larger than 100 nm with oxygen well within the particles. Based on the results, the products from the 80°C and 90°C reactions somewhat resembled monodispersed particles and could potentially result in crystal-bound cobalt sulfide particles.

The morphologies of the cobalt sulfide particles made with para-xylene-alpha-thiol and 4-trifluoromethylbenzyl mercaptan ligands were also characterized. The temperature of reaction was set to 145°C, as 200°C was too high causing the agglomeration of particles. Although 145°C is also above the boiling point of the ligands, this temperature was chosen as a control in terms of how the Me and CF_3 substituted ligands react compared to the t-Bu ligands. The morphologies that have formed do provide insight to the reactivity of the ligands. As seen in Figure 3.3d, the CF_3 ligands result in particles similar to the particles formed with the t-Bu ligands at 200°C, i.e., amorphous aggregates made up of numerous particles. The EDS (Figure 3.3f) shows that there is a uniformity of cobalt sulfide atoms within the particles, as well as oxygen being a part of the composition of particles. On the other hand, when the Me substituted ligand was used, the particles were similar to the t-Bu particles at 80 and 90°C. Interestingly, the EDS revealed the particles are actually cobalt oxide particles with sulfide atoms scattered around the perimeter of the particles.

Again, the reaction temperature is still above the boiling point of the ligands, which will likely cause the ligands to degrade. Conclusions can be drawn that less energy is required for the electronegative CF_3 substituted ligands to degrade or cleave compared to the t-Bu substituted ligands. With the Me ligands, their morphologies resemble that of the particles at low temperatures, yet did not have the same elemental composition with cobalt and oxygen. This suggests that more energy is required for Me substituted ligands to react than the t-Bu and CF_3 substituted ligands, placing the order of reactivity of the ligands to be $CF_3 >$ t-Bu $>$ Me. Based on the t-Bu temperature study, it can hypothesized that a reaction temperature below 80°C may result to cobalt sulfide particles with some sort of uniform morphology for the t-Bu and CF_3 substituted ligands, and for Me sub-

stituted ligands at temperatures slightly greater. Perhaps due to the ligands being aryl, there is less probability for there to be colloidal stability of the particles, hence less chance for monodispersity to occur, as long chain ligands are usually preferred. The effect the ligand substituents have on the formation of the cobalt sulfide particles was observed, and progression of this study can continue since these ligands are commercially available. Due to time constraints, the reaction of Me and CF_3 substituted ligands with $Co(acac)_2$ was not attempted.

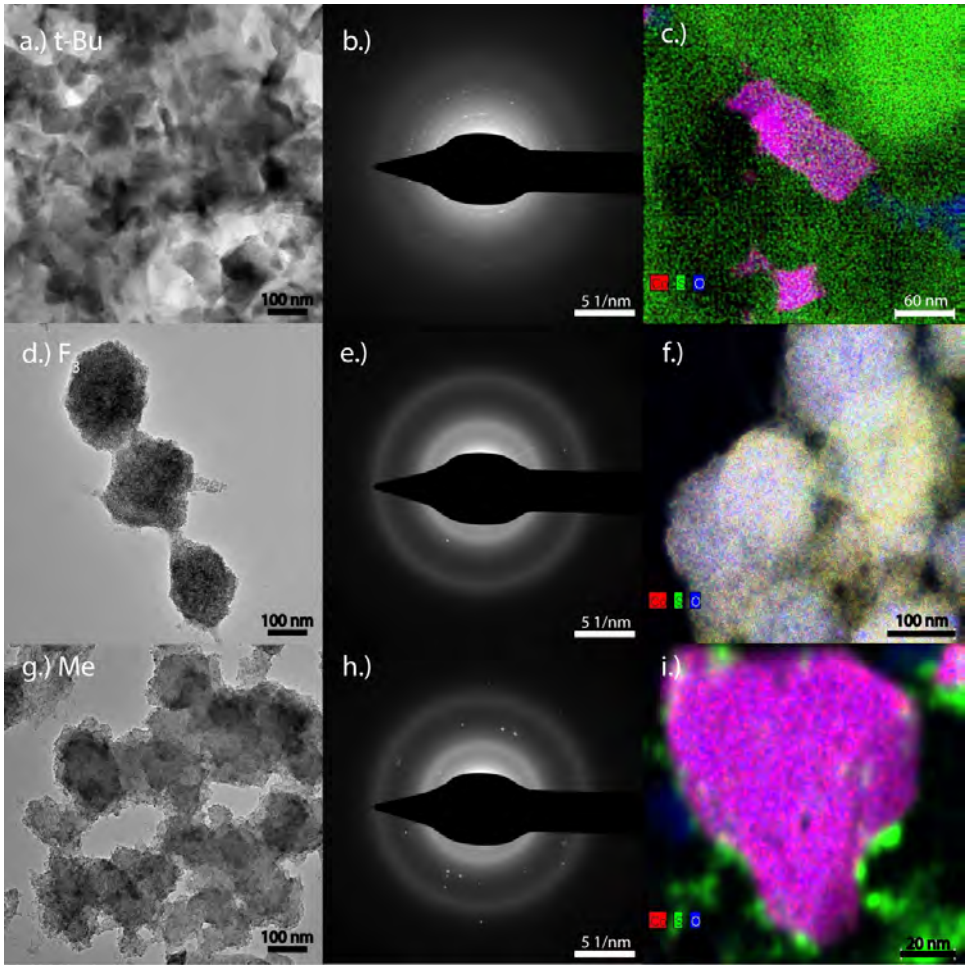

Figure 3.3. TEM, SAED, and EDS of cobalt sulfide particles synthesized at 145°C with 4-*tert*-butylbenzyl mercaptan ligands (a-c), 4-trifluoromethylbenzyl mercaptan (d-f), and para-xylene-alpha-thiol (g-i).

3.2.3 Surface Characterization of Cobalt Sulfide NPs

Before determining how the type of ligand effects the electrocatalytic activity of the cobalt sulfide particles, a general surface characterization was done on the Me, t-Bu, and CF_3 particles synthesized at 145°C. ^{1}H NMR spectra include the particles in Figure 3.4 did not reveal enough information about the surface of the particles due to the lack of colloidal stability of the particles, which ended up precipitating from solution. The signals present in the spectra is the $CDCl_3$ solvent peak at 7.26 ppm and residual ethanol peaks at 1.25 and 3.72 ppm, as well as trace water at 1.56 ppm. FT-IR was then utilized as a second surface-characterizing technique to see if it could possibly reveal more information on the ligands on the surface, or if there were any ligands present.

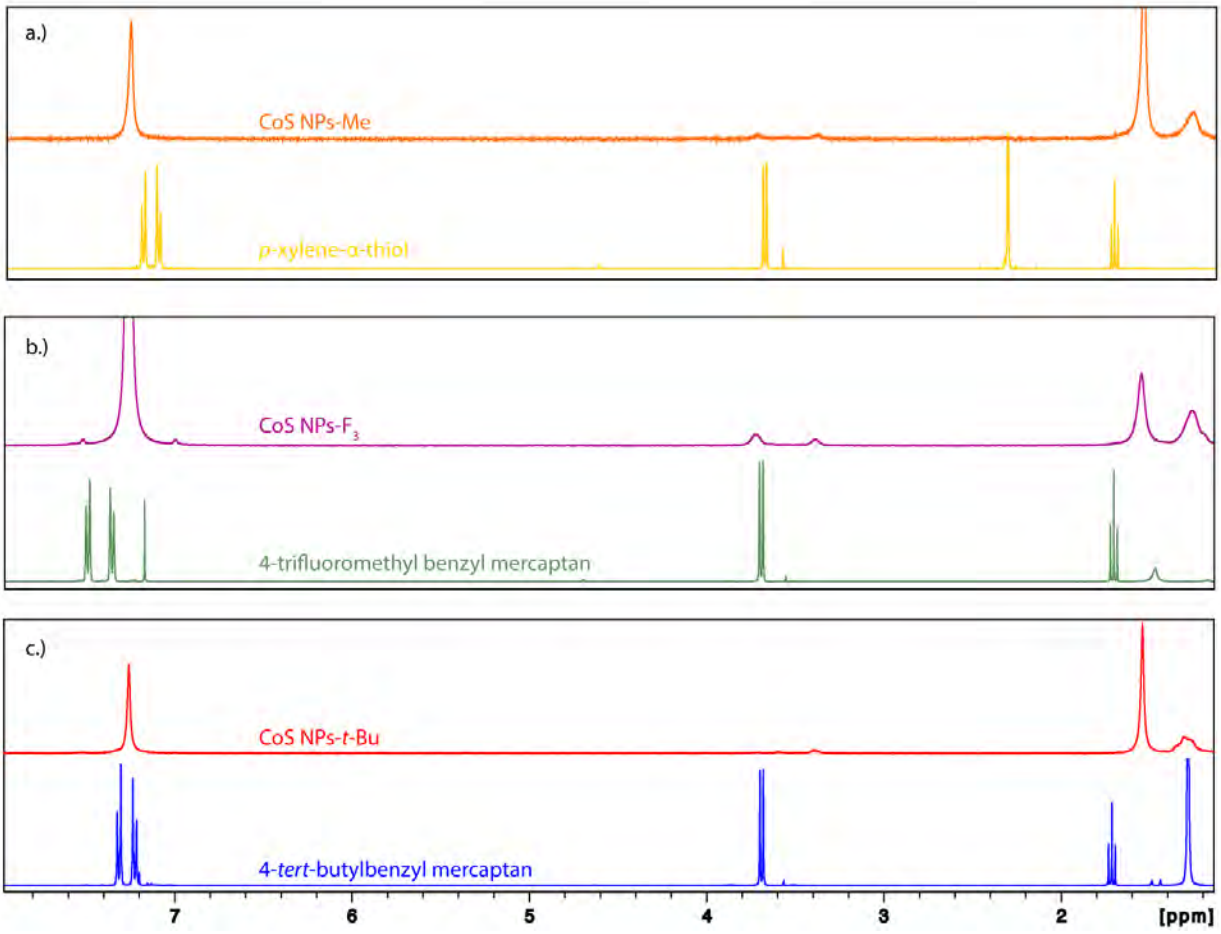

Figure 3.4. ^{1}H NMR spectra of the as synthesized cobalt sulfide particles with a.) para-xylene-alpha-thiol, b.) 4-trifluoromethylbenzyl mercaptan, and c.) 4-*tert*-butylbenzyl mercaptan ligands and their respective pure ligand NMR.

In the FT-IR spectra of cobalt sulfide particles with Me substituted ligands (Figure 3.5-bottom), the strong peak at 750 and 1213 cm^{-1} coincide with the out-of-plane (oop) and in plane bending of the =C–H on a para substituted aromatic, respectively. The aromatic C=C stretch at 1420 and 1512 cm^{-1} is seen along with the sp^2 C–H stretch, which is a relatively medium peak at 3018 cm^{-1}. The weak peak at 2920 and 2975 cm^{-1} could either be attributed to the symmetric and asymmetric sp^3 C–H stretch of the CH_2–the SH or the aromatic CH_3. The broad peak around 3300 cm^{-1} could be a result of ethanol still present after the washing of the particles. The FT-IR spectra of the CF_3 substituted ligands (Figure 3.5-middle) was mainly featureless with a medium intense peak at 1324 cm^{-1} from the C–F_3 stretching. As for the t-Bu substituted ligand (Figure 3.5-top), the strong peak at 752 cm^{-1} could be the oop =C–H bending of the para-substituted aromatic with the in-plane bending peaks at 1045 and 1087 cm^{-1}. The medium peaks at 1215 and 1267 cm^{-1} pertain to the C–C stretch of the *tert*-butyl, with the small to medium peaks attributed to the sp^3 C–H stretches at 2869, 2900, and 2967 cm^{-1}. The weak peak at 3011 cm^{-1} is the aromatic sp^2 C–H stretch, whereas the strong broad peak at 3300 cm^{-1} is free hydroxide.

The presence of an OH could either be from impurities or it actually being on the surface of the particles as oxygen atoms are very much a part of the particle composition. Taking a closer look at the FI-IR spectra of both the Me and t-Bu, the strong oop peak at 750 cm^{-1} raises some questions. Usually, the oop for para substituted aromatics is above 800 cm^{-1}, where ortho-substituted aromatics have a strong peak around 750 cm^{-1}. Because of the high reaction temperature, there might be a rearrangement occurring resulting in the isomerization of the aryl thiol ligands, or the formation of some type of disulfide. The lack of structure and colloidal stability limited the ability to obtain a well-characterized surface of the cobalt sulfide particles in both the ^1H NMR and FT-IR spectra. This is why surface characterization of nanoparticles is difficult, as not all spectroscopies and techniques may give enough information to draw a conclusion about how the ligands are bound to the surface. So far, it can be assumed that the ligands are present, but the binding mode can not directly determined. The FT-IR can provide as a control for comparison for the cobalt sulfide particles made at lower temperatures.

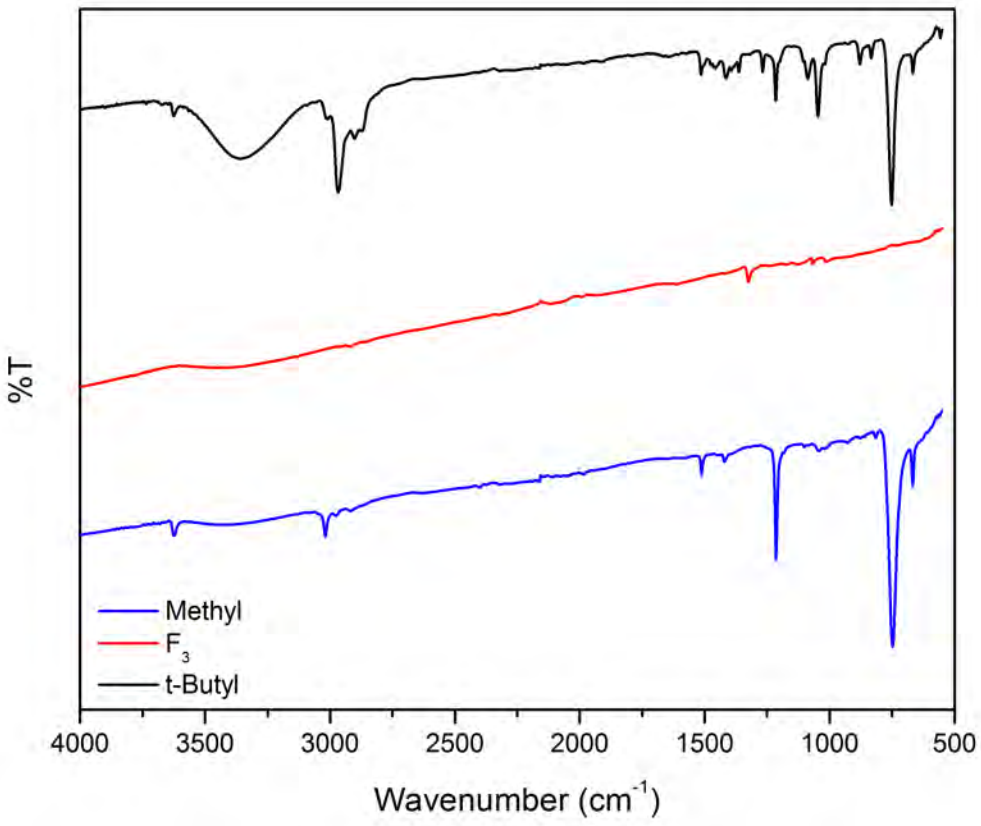

Figure 3.5. FT-IT spectra of the as synthesized cobalt sulfide particles with a.) para-xylene-alpha-thiol (blue/bottom) b.) 4-trifluoromethylbenzyl mercaptan (red/middle), and c.) 4-*tert*-butylbenzyl mercaptan ligands (black/top).

3.2.4 HER Activity of Cobalt Sulfide Particles

Linear sweep voltammetry (LSV) is commonly used to evaluate the HER performance by measuring the catalytic current as a function of potential. The HER activity of the as-synthesized cobalt sulfide particles is evaluated here, as the electrocatalytic activity of cobalt sulfide and cobalt chalcogenides has been previously investigated.[70,72,75,76] The electrocatalytic activity of the cobalt sulfide particles with the t-Bu ligands synthesized at 145°C was measured by drop casting the particles on the surface of a glassy carbon working electrode and allowing them to dry in air. LSV was carried out in an acidic electrolyte of 0.5M H_2SO_4 at a scan rate of 50 $mV{\cdot}s^{-1}$ with a 1 mV voltage step from 0 to -0.70 V vs. Ag/AgCl. In Figure 3.6, the first sweep appears to have some features suggesting there might be multiple activities occurring between the electrode and acidic

electrolyte. As the sweeps continue, the rate begins to decrease and the curve's features begin to flatten, which might be due to the particle's degrading. This data is from one trial, so no conclusion can be drawn until more trials are done.

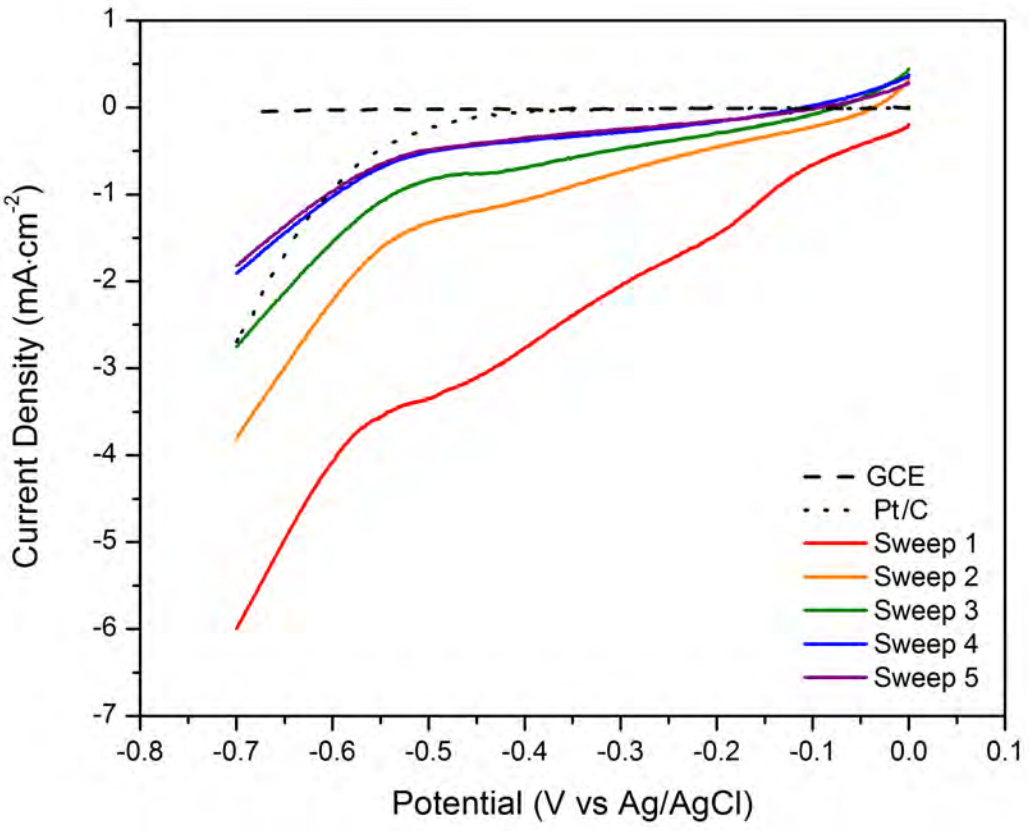

Figure 3.6. Polarization curve of cobalt sulfide particles with t-Bu ligands synthesized at 145°C in the acidic electrolyte of 0.5M H_2SO_4. Glassy carbon and Pt working electrodes were used as controls.

3.3 Future Direction

The study of cobalt sulfide is still in its infancy, and further studies are needed to determine how the substitutional group of ligands affect the electrocatalytic activity and whether there is any catalytic advantage to having crystal-bound ligands. Ligands containing an electron-withdrawing group on the aryl thiol ligands are very reactive at low temperatures, which could potentially be of use in synthesizing cobalt sulfide NPs. Control over the phase and morphology of cobalt sulfide particles is difficult to obtain, and have yet to produce particles within the nano regime because of

the complicated phase diagram of cobalt sulfides. Due to cobalt's high affinity for oxygen and the reduction potential of sulfides, a metal precursor that does not contain oxygen may be beneficial in preventing the incorporation of oxygen within the particles.

CHAPTER 4

SUMMARY AND FUTURE DIRECTION

Catalysis continues to play an essential role in increasing the rate of production for U.S. chemical industries. Heterogenous catalysts are sought after due to their relative ease of separation from the product, allowing for catalytic recyclability. Nanomaterials continue to be integrated into chemical syntheses because of their high surface-to-volume ratio, which makes them effective heterogeneous catalysts. Interest in the use of compound metal nanoparticles for catalysis has increased, as they have been reported to be efficient catalysts for redox, coupling, and electrochemical reactions. The metals in the CMNPs are traditionally noble and late transition metals, but their scarcity and cost restrict their application in large-scale catalytic processes. As a result, focus has shifted towards using first-row transition metals with carbides, nitrides, sulfides, or phosphides, which are environmentally friendly, inexpensive, and earth abundant.

The bottom-up syntheses of CMNPs enables modification of their morphology, size, composition, structure, and surface chemistry, which ultimately changes the nanomaterial's catalytic properties. These modifications to nanomaterials lead to the exposure of different facets, which can increase or decrease the number of metals available in the catalytic reaction. Ligands, surfactants, and polymers are used in the synthesis of CMNPs, as they lower the surface energy, thereby promoting nucleations of small NPs. CMNP shape and facet exposure can be controlled by ligands, where the type of ligand used can affect the catalytic activity negatively by blocking the metal sites and preventing a reaction from occurring on the surface.

An alternative ligand binding mode can be accessed when the ligand is also the anion source and stabilizing agent; this binding mode has been termed "crystal-bound". The ligands sit in higher coordination number sites, forming a terminal layer and are expected to allow exposure of the active metal sites. Control of the exposed facets is crucial and can be challenging when the surface of CMNPs are not well-characterized prior to use as catalysts. The overall theme of this

thesis was to prepare nickel phosphine and cobalt sulfide NPs with crystal-bound ligands, and to determine the effect of the type of ligand used and the reaction temperature on the binding mode of the ligands.

4.1 Summary

Ni_xP_y NPs have already been introduced as heterogeneous catalysts for water splitting, water oxidation, hydrogen evolution, hydrodeoxygenation, and hydrodesulfurization processes. There is a lack of surface characterization of these NPs prior to their use as catalysts, despite the importance of surface chemistry in heterogeneous processes. Ni_xP_y NPs have been synthesized via hydrothermal, solvothermal, and organometallic decomposition routes at reaction temperatures greater than 300°C. Ni_xP_y NPs used for hydrodesulfurization processes have previously been synthesized via thermal decomposition, wherein an organometallic compound or metal salt is the metal precursor, and phosphine ligands are the anion source. Tributylphosphine, trioctylphosphine, and triphenylphosphine were the ligands implemented as the anion source, and their effects on morphology, size, composition, and structure were characterized prior to surface characterization of the resulting NPs.

All three phosphine ligands resulted in pure phase Ni_2P pseudo-spherical NPs. An increase in size from TBP $<$ TOP $<$ TPP was a result of the changes in P–C bond strength and steric hinderance of the respective ligands. The surface characterization via ^{1}H NMR of the as-synthesized Ni_2P NPs with TBP, TOP, and TPP showed that there were phosphine ligands on the surface, as the vinyl to methyl proton integration of oleylamine did not equal 2H:3H. A successful ligand exchange with a competitive L-type ligand led to the conclusion that none of the phosphine ligands were crystal-bound. Since the reaction temperature of 320°C is higher than the boiling points of the ligands, the reaction temperature of the NPs was decreased from 265–300°C in an effort to obtain crystal-bound ligands.

The temperature study of Ni_2P NPs revealed that the mechanism of formation is likely more complicated that then mechanism reported in literature. The new proposed mechanism of forma-

tion, supported by EDS, begins with the nucleation of Ni seeds at 265°C, followed by P–C cleavage of the phosphine ligands, resulting in core-shell Ni/Ni_5P_2 NPs. Once the temperature reaches 285°C, diffusion of P atoms into the Ni seeds is successful and $Ni_{12}P_5$/Ni_2P phases are present. Saturation of P atoms into the seeds is observed from 285–320°C. The rapid P–C cleavage occurs at temperatures greater than 285°C, whereas at 275°C there is enough energy to cleave the P–C bonds, but not enough for complete diffusion of P atoms into the Ni seeds. As the temperature increases and more phosphine ligands are depleted, oleylamine becomes the NP stabilizing agent. This conclusion is supported by the ^{1}H NMR temperature spectra. The NPs formed at 275°C are more likely to have crystal-bound ligands, but due to the magnetic behavior of the Ni core, the ^{1}H NMR was featureless.

The surface characterization of cobalt sulfide particles was more difficult to obtain than that of Ni_2P, as the solvothermal reaction of cobalt (II) acetylacetonate in the presence of an primary aryl thiol ligand resulted in amorphous particles larger than 100 nm. Due to the high affinity of cobalt for oxygen and the reduction potential of sulfide, there was a significant amount of oxygen present within the particles. Little information about the NP surface chemistry was obtained by the ^{1}H NMR due to colloidal instability. The effect of the substituted functional group on the aryl thiol ligands was also evaluated. The more electron-withdrawing the substituted functional group was, the more reactive it was in forming more compact particles. In this case, the most electron-withdrawing substituent was the trifluoromethyl group in the para position, and it was more reactive than the *tert*-butyl and methyl substituents, in accordance with this trend. FT-IR suggests that the thiol ligands may be isomerizing at a reaction temperature of 145°C, since the out-of-plane bending of the aryl thiol correlates more strongly with an ortho-substituted aryl thiol than a para-substituted aryl. Furthermore, the hydrogen evolution activity of the cobalt sulfide particles synthesized at 145°C in the presence of an aryl thiol substituted with *tert*-butyl ligands was briefly studied via LSV. Only one trial was recorded, so no conclusions could be drawn.

4.2 Outlook

The work that was performed in chapter 2 revealed that when Ni_2P NPs are synthesized with an alkyl phosphine and oleylamine ligands, both ligands are present on the surface. However, their binding mode has yet to be characterized. One possible route to determine their binding mode would be through ligand exchange with a competitive L-type ligand, such as in section 2.3.2. If the ligands are crystal-bound, then the respective proton peaks of the initial ligand would remain, as the ligand used for exchange would be removed during the cleaning of the NPs. FT-IR and TGA-MS could be employed to evaluate the binding-mode of the ligands by comparing the results obtained to that of Ni_2P NPs synthesized at 320°C, as they are known to be surface-bound. If the ligands are crystal-bound, there should be a distinct difference in the stretches in the FT-IR between surface and crystal-bound ligands. There would also be a difference in mass loss between the two binding modes for TGA-MS. Cobalt sulfide experiments performed in chapter 3 revealed the challenge that other researchers have encountered in the attempt to make monodispersed single phase cobalt sulfide nanoparticles. These studies are still in their infancy, but optimization of the synthesis is required to form crystalline particles as this would facilitate detailed characterization of the surface and modification thereof. Although there have been reports that amorphous cobalt sulfide particles still exhibit catalytic activity, crystalline particles (i) can provide a controlled foundation when modifying the surface of the NPs; and (ii) would allow a correlation to be made between the crystal faces exposed and catalytic activity.

Since heterogeneous catalysts are highly dependent on their surface characteristics, control of NPs growth to expose catalytic active facets is essential when generating CMNPs catalysts. There is still a desire in achieving ligands that are crystal-bound for all CMNPs, as this could potentially increase catalytic efficiency while eliminating the need for exterior supports. If this binding mode can not be reached for all CMNPs, detailed characterization should still be a requirement prior to testing their catalytic activity in order to fully understand the chemistry that occurs on the surface of the NPs in a chemical reaction. If the ligands can be tailored to form a crystal-binding mode, this can lead to the design of ligands that incorporate a chiral center, inducing enantioselectivity.

In the absence of a chiral environment, traditional chemical synthesis processes yield racemic mixtures of the two enantiomers of synthetic chiral compounds. As a result, enantioselective chemical processing in chiral media is an important subject of research in the pharmaceutical industries. This is largely due to the fact that two enantiomers of a chiral molecule can have vastly different physiological properties. For example, one enantiomer could target a specific cell, whereas the other could result in unwanted side effects. Enantioselectivity in heterogeneous processes is desired as it can reduce waste and increase the yield of a specific product. Thin chiral metal sheets with a specific facet have shown to be enantioselective towards amino acids, but this has yet to be accomplished on CMNPs.[77–80] Gold nanoparticles and some quantum dots have been modified with chiral amino acids on the surface, leading to enantioselective adsortion and separation. These studies can be used as a guide in the experimental design of chiral crystal-bound ligands in CMNPS.[81–83]

Technology is constantly evolving as well as the characterization techniques used for nanomaterials. As the demand for efficient and quick heterogeneous chemical processes grows to meet the fundamental needs of society, having a fundamental understanding of the growth and surface of nanomaterials will allow for compound metal nanoparticles to be tailored for specific reactions. Whether that is through a new crystal binding mode or with just a detailed characterization of the ligands present on the surface, efficient CMNPs with high catalytic properties can be achieved.

APPENDIX A

SUPPLEMENTARY MATERIAL FOR CHAPTER 3

A.1 Experimental Techniques

A.1.1 Materials

Dioctylether (DOE, 99%), para-xylene-alpha-thiol, 4-trifluoromethylbenzyl mercaptan, 4-*tert*-butylbenzyl mercaptan, and cobalt (II) acetylacetonate hydrate ($Co(acac)_2$) were purchased from Sigma-Aldrich. All chemicals were used as received without additional purification unless noted. Standard air-free Schlenk techniques were used throughout with N_2 as the inert gas

A.1.2 Synthesis of Cobalt Sulfide NPs

A synthesis was developed based on the work of Robinson *et al.*[60] $Co(acac)_2$ (1.0 mmol) was added to DOE (5.00 mL) in a three-neck round-bottom flask. The reaction mixture degased for 1 h at 80°C, and then increased to the desired temperature (80 – 200°C) under a $N_{2(g)}$ atmosphere. At peak temperature 2.0 mmol of para-xylene-alpha-thiol, 4-trifluoromethylbenzyl mercaptan, or 4-*tert*-butylbenzyl mercaptanwas was injected and then stirred for 1 h. The reaction was cooled to ambient temperature by the removal of the heat source. A 2.0 mL portion of chloroform/toluene (1:1) was added to the reaction mixture in air followed by 15 min of sonication. The NPs were precipitated by the addition of 30.0 mL of ethanol, and separated via centrifugation at 8700 rpm for 10 min. The NPs were further purified by repeated centrifugation and decantation with additions of ethanol and minimal chloroform.

A.1.3 Characterization & Instrumentation

TEM and EDS mapping data were collected using a FEI Tecnai Osiris™ digital 200 kV S/TEM system equipped with ChemiSTEM EDS. TEM samples were prepared by drop casting a dilute

NP solution in chloroform onto a copper grid with a carbon support and dried in air at room temperature. EDS spectra were collected for 2 min and quantified using the Espirit software. S content was quantified using the K series of peaks, while Co content was quantified using the L series. All spectra were background subtracted and overlapping Co sample and Cu grid peaks were deconvoluted before quantification. Drift-corrected EDS maps were collected for 90 s with beam current 1.5 nA.

XRD measurements were performed using a Rigaku X-ray diffractometer with a CuK_α (λ = 0.154 nm) radiation source. The resulting diffraction patterns were then visually compared to data from the ICDD database and literature examples to determine the structure. The absorption spectra of NP samples were collected from 300–1000 nm on a UV-Vis spectrophotometer (Jasco V-670) with an excitation wavelength of 348 nm. Samples were measured in solution with chloroform as the solvent. ^{1}H NMR spectra were recorded on Bruker DRX-400 (400 MHz) spectrometers. Spectra were calibrated to residual solvent signals of 7.26 ppm for ^{1}H NMR spectra in $CDCl_3$. FTIR spectra were collected using a Thermo Scientific™ Nicolet™ iS™5 FT-IR spectrometer driven by Thermo Scientific™ OMNIC™ software.

A.1.4 Electrochemical Measurements

The HER activity of the as-synthesized CoS particles was measured in a standard three-electrode system controlled by Gamry Series G 300 instrument with PHE200 & EIS300 Software Packages. The working electrode was prepared by drop casting an aliquot of a CoS solution onto a glass carbon electrode (GCE, 4 mm in diameter), and dried at room temperature. CoS/GCE was submerged into 25.0 mL of 0.5M H_2SO_4 along with a Ag/AgCl reference electrode (saturated KCl) and Pt mesh counterelectrode. Linear sweep voltammetry (LSV) was carried out at a scan rate of 50 $mV \cdot s^{-1}$ with a 1 mV voltage step from 0 to -0.70 V vs. Ag/AgCl.

REFERENCES

1. National Research Council, *Catalytic Process Technology*; National Academies Press: Washington, D.C., 2000.

2. Oleson, J.; Haynes, V.; Ramaker, B.; Slough, R.; Whalen, H.; Sciance, T.; Saft, M.; Jost, D.; Tamerelli, W.; Turner, S.; Brooks, D.; Artemis, D.; Kellogg, D. *Technology Vision 2020*; 1996; pp 1–75.

3. Fechete, I.; Wang, Y.; Védrine, J. C. *Catal. Today* **2012**, *189*, 2–27.

4. Deikus, G.; Bechhofer, D. H. *J. Biol. Chem.*, 40th ed.; Courier Corporation, 2011; Vol. 286; pp 34932–34940.

5. Hammer, B. *Top. Catal.* **2006**, *37*, 3–16.

6. Zaera, F. *Chem. Soc. Rev.* **2013**, *42*, 2746–2762.

7. Boles, M. A.; Engel, M.; Talapin, D. V. *Chem. Rev.* **2016**, *116*, 11220–11289.

8. Polte, J. *CrystEngComm* **2015**, *17*, 6809–6830.

9. Mori, K.; Yamashita, H. *RSC Catal. Ser. No. 17*, 17th ed.; Royal Society of Chemistry, 2014; pp 30–46.

10. Campelo, J. M.; Luna, D.; Luque, R.; Marinas, J. M.; Romero, A. A. *ChemSusChem* **2009**, *2*, 18–45.

11. Menezes, P. W.; Indra, A.; Das, C.; Walter, C.; Gobel, C.; Gutkin, V.; Schmeiber, D.; Driess, M. *ACS Catal.* **2017**, *7*, 103–109.

12. Guan, Q.; Cheng, X.; Li, R.; Li, W. *J. Catal.* **2013**, *299*, 1–9.

13. Wang, J.; Gu, H. *Molecules* **2015**, *20*, 17070–17092.

14. Alexander, A.-M.; Hargreaves, J. S. J. *Chem. Soc. Rev.* **2010**, *39*, 4388.

15. Carenco, S.; Portehault, D.; Boissière, C.; Mézailles, N.; Sanchez, C. *Chem. Rev.* **2013**, *113*, 7981–8065.

16. Yan, N.; Xiao, C.; Kou, Y. *Coord. Chem. Rev.* **2010**, *254*, 1179–1218.

17. Liu, P. *RSC Catal. Ser.*, 17th ed.; Royal Society of Chemistry, 2014; pp 219–234.

18. Krishna Perala, S. R.; Kumar, S. *Langmuir* **2014**, *30*, 12703–12711.

19. Thanh, N. T. K.; Maclean, N.; Mahiddine, S. *Chem. Rev.* **2014**, *114*, 7610–7630.

20. Shiju, N. R.; Guliants, V. V. *Appl. Catal. A Gen.* **2009**, *356*, 1–17.

21. Liu, P.; Qin, R.; Fu, G.; Zheng, N. *J. Am. Chem. Soc.* **2017**, *139*, 2122–2131.

22. Dai, Y.; Wang, Y.; Liu, B.; Yang, Y. *Small* **2015**, *11*, 268–289.

23. Boles, M. a.; Ling, D.; Hyeon, T.; Talapin, D. V. *Nat. Mater.* **2016**, *15*, 364–364.

24. Duran Pachon, L.; Rothenberg, G. *Appl. Organomet. Chem.* **2008**, *22*, 288–299.

25. Astruc, D.; Lu, F.; Aranzaes, J. R. *Angew. Chem. Int. Ed.* **2005**, *44*, 7852–7872.

26. Niu, Z.; Li, Y. *Chem. Mater.* **2014**, *26*, 72–83.

27. Turo, M. J.; Macdonald, J. E. *ACS Nano* **2014**, *8*, 10205–13.

28. Turo, M. J.; Shen, X.; Brandon, N. K.; Castillo, S.; Fall, A. M.; Pantelides, T.; Macdonald, J. E. *Chem. Commun.* **2016**, *52*, 12214–12217.

29. Shen, Y.; Gee, M. Y.; Greytak, A. B. *Chem. Commun.* **2017**, *53*, 827–841.

30. Cecilia, J.; Infantes-Molina, A.; Rodriguez-Castellon, E.; Jimenez-Lopez, A. *J. Catal.* **2009**, *263*, 4–15.

31. Callejas, J. F.; Read, C. G.; Roske, C. W.; Lewis, N. S.; Schaak, R. E. *Chem. Mater.* **2016**, *28*, 6017–6044.

32. Jiang, N.; You, B.; Sheng, M.; Sun, Y. *ChemCatChem* **2016**, *8*, 106–112.

33. Liang, H.; Gandi, A. N.; Anjum, D. H.; Wang, X.; Schwingenschlögl, U.; Alshareef, H. N. *Nano Lett.* **2016**, *16*, 7718–7725.

34. Li, D.; Baydoun, H.; Verani, C. N.; Brock, S. L. *J. Am. Chem. Soc.* **2016**, *138*, 4006–4009.

35. Han, A.; Chen, H.; Sun, Z.; Xu, J.; Du, P. *Chem. Commun.* **2015**, *51*, 11626–11629.

36. Chen, G.; Xu, C.; Huang, X.; Ye, J.; Gu, L.; Li, G.; Tang, Z.; Wu, B.; Yang, H.; Zhao, Z.; Zhou, Z.; Fu, G.; Zheng, N. *Nat. Mater.* **2016**, *15*, 564–569.

37. Feng, L.; Vrubel, H.; Bensimon, M.; Hu, X. *Phys. Chem. Chem. Phys.* **2014**, *16*, 5917.

38. Ha, D.-h.; Han, B.; Risch, M.; Giordano, L.; Yao, K. P.; Karayaylali, P.; Shao-Horn, Y. *Nano Energy* **2016**, *29*, 37–45.

39. Laursen, A. B.; Patraju, K. R.; Whitaker, M. J.; Retuerto, M.; Sarkar, T.; Yao, N.; Ramanujachary, K. V.; Greenblatt, M.; Dismukes, G. C. *Energy Environ. Sci.* **2015**, *8*, 1027–1034.

40. Wan, L.; Zhang, J.; Chen, Y.; Zhong, C.; Hu, W.; Deng, Y. *Int. J. Hydrogen Energy* **2016**, *41*, 20515–20522.

41. Koike, N.; Hosokai, S.; Takagaki, A.; Nishimura, S.; Kikuchi, R.; Ebitani, K.; Suzuki, Y.; Oyama, S. T. *J. Catal.* **2016**, *333*, 115–126.

42. Habas, S. E.; Baddour, F. G.; Ruddy, D. A.; Nash, C. P.; Wang, J.; Pan, M.; Hensley, J. E.; Schaidle, J. A. *Chem. Mater.* **2015**, *27*, 7580–7592.

43. D'Aquino, A. I.; Danforth, S. J.; Clinkingbeard, T. R.; Ilic, B.; Pullan, L.; Reynolds, M. A.; Murray, B. D.; Bussell, M. E. *J. Catal.* **2016**, *335*, 204–214.

44. Duan, X.; Teng, Y.; Wang, A.; Kogan, V.; Li, X.; Wang, Y. *J. Catal.* **2009**, *261*, 232–240.

45. Tamang, S.; Lincheneau, C.; Hermans, Y.; Jeong, S.; Reiss, P. *Chem. Mater.* **2016**, *28*, 2491–2506.

46. Kim, Y.-H.; Jun, Y.-w.; Jun, B.-H.; Lee, S.-M.; Cheon, J. *J. Am. Chem. Soc.* **2002**, *124*, 13656–13657.

47. Li, D.; Senevirathne, K.; Aquilina, L.; Brock, S. L. *Inorg. Chem.* **2015**, *54*, 7968–7975.

48. Prins, R.; Bussell, M. E. *Catal. Letters* **2012**, *142*, 1413–1436.

49. Oyama, S. T.; Gott, T.; Zhao, H.; Lee, Y.-K. *Catal. Today* **2009**, *143*, 94–107.

50. Liu, P.; Rodriguez, J. A.; Asakura, T.; Gomes, J.; Nakamura, K. *J. Phys. Chem. B* **2005**, *109*, 4575–4583.

51. Le Val Duchesse, *The importance of nickel compounds: catalysts*; 2007; pp 1–5.

52. Liu, J.; Chen, X.; Shao, M.; An, C.; Yu, W.; Qian, Y. *J. Cryst. Growth* **2003**, *252*, 297–301.

53. Luo, Z.-Z.; Zhang, Y.; Zhang, C.; Tan, H. T.; Li, Z.; Abutaha, A.; Wu, X.-L.; Xiong, Q.; Khor, K. A.; Hippalgaonkar, K.; Xu, J.; Hng, H. H.; Yan, Q. *Adv. Energy Mater.* **2017**, *7*, 1601285.

54. Mi, K.; Ni, Y.; Hong, J. *J. Phys. Chem. Solids* **2011**, *72*, 1452–1456.

55. Chiang, R.-K.; Chiang, R.-t. *Inorg. Chem.* **2007**, *46*, 369–371.

56. Pan, Y.; Lin, Y.; Liu, Y.; Liu, C. *Appl. Surf. Sci.* **2016**, *366*, 439–447.

57. Sobhani, A.; Salavati-Niasari, M. *J. Mater. Sci. Mater. Electron.* **2016**, *27*, 3619–3627.

58. Duan, H.; Yuan, S.; Zheng, X.; Tian, Z. *J. Wuhan Univ. Technol. Sci. Ed.* **2013**, *28*, 467–470.

59. Seo, B.; Baek, D. S.; Sa, Y. J.; Joo, S. H. *CrystEngComm* **2016**, *18*, 6083–6089.

60. Robinson, E. H.; Turo, M. J.; Macdonald, J. E. *Chem. Mater.* **2017**, *29*, 3854–3857.

61. De Roo, J.; Van Driessche, I.; Martins, J. C.; Hens, Z. *Nat. Mater.* **2016**, *15*, 517–521.

62. Chen, O.; Zhao, J.; Chauhan, V. P.; Cui, J.; Wong, C.; Harris, D. K.; Wei, H.; Han, H.-S.; Fukumura, D.; Jain, R. K.; Bawendi, M. G. *Nat. Mater.* **2013**, *12*, 445–451.

63. Frederick, M. T.; Achtyl, J. L.; Knowles, K. E.; Weiss, E. A.; Geiger, F. M. *J. Am. Chem. Soc.* **2011**, *133*, 7476–7481.

64. Zafiropoulou, I.; Papagelis, K.; Boukos, N.; Siokou, A.; Niarchos, D.; Tzitzios, V. *J. Phys. Chem. C* **2010**, *114*, 7582–7585.

65. Seo, H.-R.; Cho, K.-S.; Lee, Y.-K. *Mater. Sci. Eng. B* **2011**, *176*, 132–140.

66. Henkes, A. E.; Vasquez, Y.; Schaak, R. E. *J. Am. Chem. Soc.* **2007**, *129*, 1896–1897.

67. Mahmood, N.; Zhang, C.; Jiang, J.; Liu, F.; Hou, Y. *Chem. Eur. J.* **2013**, *19*, 5183–5190.

68. Lauritsen, J.; Besenbacher, F. *J. Catal.* **2015**, *328*, 49–58.

69. Liu, C.; Liu, H.; Yin, C.; Zhao, X.; Liu, B.; Li, X.; Li, Y.; Liu, Y. *Fuel* **2015**, *154*, 88–94.

70. Cai, P.; Huang, J.; Chen, J.; Wen, Z. *Angew. Chem. Int. Ed.* **2017**, *56*, 4858–4861.

71. Dou, S.; Tao, L.; Huo, J.; Wang, S.; Dai, L. *Energy Environ. Sci.* **2016**, *9*, 1320–1326.

72. Cui, Y.; Zhou, C.; Li, X.; Gao, Y.; Zhang, J. *Electrochim. Acta* **2017**, *228*, 428–435.

73. Bao, S.-J.; Li, Y.; Li, C. M.; Bao, Q.; Lu, Q.; Guo, J. *Cryst. Growth Des.* **2008**, *8*, 3745–3749.

74. Sibokoza, S. B.; Moloto, M. J.; Moloto, N.; Sibiya, P. N.; Africa, S. *Chalcogenide Lett.* **2017**, *14*, 69–78.

75. Kornienko, N.; Resasco, J.; Becknell, N.; Jiang, C. M.; Liu, Y. S.; Nie, K.; Sun, X.; Guo, J.; Leone, S. R.; Yang, P. *J. Am. Chem. Soc.* **2015**, *137*, 7448–7455.

76. Nelson, A.; Fritz, K. E.; Honrao, S.; Hennig, R. G.; Robinson, R. D.; Suntivich, J. *J. Mater. Chem. A* **2016**, *4*, 2842–2848.

77. Mahapatra, M.; Tysoe, W. T. *J. Phys. Chem. C* **2016**, *120*, 2309–2319.

78. Yun, Y.; Gellman, A. J. *Langmuir* **2015**, *31*, 6055–6063.

79. Raval, R. *J. Mol. Catal. A Chem.* **2009**, *305*, 112–116.

80. Nicklin, R. E. J.; Cornish, A.; Shavorskiy, A.; Baldanza, S.; Schulte, K.; Liu, Z.; Bennett, R. A.; Held, G. *J. Phys. Chem. C* **2015**, *119*, 26566–26574.

81. Shukla, N.; Bartel, M. A.; Gellman, A. J. *J. Am. Chem. Soc.* **2010**, *132*, 8575–8580.

82. Choi, J. K.; Haynie, B. E.; Tohgha, U.; Pap, L.; Elliott, K. W.; Leonard, B. M.; Dzyuba, S. V.; Varga, K.; Kubelka, J.; Balaz, M. *ACS Nano* **2016**, *10*, 3809–3815.

83. Baddeley, C. *Top. Catal.* **2003**, *25*, 17–28.